Journal of Marine Systems 187 (2018) 206–222

Contents lists available at ScienceDirect

Journal of Marine Systems

journal homepage: www.elsevier.com/locate/jmarsys

Sensitivity of the Bay of Bengal upper ocean to different winds and river input conditions

Sudip Jana[a,*], Avijit Gangopadhyay[b], Pierre F.J. Lermusiaux[a], Arun Chakraborty[c], Sourav Sil[d], Patrick J. Haley Jr.[a]

[a] Department of Mechanical Engineering, Massachusetts Institute of Technology, USA
[b] School for Marine Science and Technology, University of Massachusetts Dartmouth, USA
[c] Centre for Oceans, Rivers, Atmosphere and Land Sciences, Indian Institute of Technology Kharagpur, India
[d] School of Earth, Ocean and Climate Sciences, Indian Institute of Technology Bhubaneswar, India

ARTICLE INFO

Keywords:
Bay of Bengal
Sensitivity study
Winds and rivers
Stratification and barrier layer
Circulation
Coastal upwelling

ABSTRACT

The sensitivity of the Bay of Bengal (BoB) upper ocean circulation and thermohaline structure to varying wind strengths and river salinity conditions is investigated using a set of long-term mesoscale simulations. The Regional Ocean Modeling System (ROMS) simulations differ in their forcing fields for winds (strong vs. weak) and in their representations of river input salinity conditions (seasonally varying estuarine salinity vs. zero salinity). The sensitivities are analyzed in terms of the responses of the surface circulation, thermohaline structure, freshwater plume dispersion, and the coastal upwelling along the western boundary. All the simulations reproduce the main broad-scale features of the Bay, while their magnitudes and variabilities depend on the forcing conditions. The impact of stronger wind is felt at greater depths for temperature than for salinity throughout the domain; however, the impact is realized with vertical distributions that are different in the northern than in the southern Bay.

As expected, the stronger wind-induced enhanced mixing lowers (enhances) the upper ocean temperature (salinity) by 0.2 °C (0.3 psu), and weakens the near-surface stratification. Moreover, stronger wind enhances eddy activity, strengthens the springtime Western Boundary Current (WBC) and enhances coastal upwelling during spring and summer along the east coast of India. The fresher river input reduces the surface salinity and hence enhances the spreading and intensity of the freshwater plume, stratification, and barrier layer thickness. The lower salinity simulation leads to an eddy-dominant springtime WBC, and enhances the freshness, strength, and southward extent of the autumn East India Coastal Current (EICC). The stronger wind simulations appear to prevent the spreading of the freshwater plume during the summer monsoon due to enhanced mixing. Fresher river input reduces the overall surface salinity by ~0.4 psu; however, it significantly underestimates the salinity near the river mouths, whereas the estuarine salinity river input simulations are closer to reality. These results highlight the importance of river input salinity and realistic strong winds in reducing model biases of high-resolution simulations for the Bay of Bengal.

1. Introduction

The circulation of the Bay of Bengal (BoB) receives major contributions from both wind and river forcing. While the seasonally reversing winds force seasonally reversing boundary currents and opposing gyre circulations in spring and autumn (Cutler and Swallow, 1984; Hastenrath and Greischar, 1991; McCreary et al., 1993; Schott et al., 2009; Durand et al., 2009; Gangopadhyay et al., 2013 and references therein), the large freshwater discharge from the adjoining rivers introduces one of the largest salinity contrasts (Fig. 1) in the tropical ocean (Varkey et al., 1996; Thadathil et al., 2002; Jana et al., 2015 and references therein). The freshwater cap in the surface layers leads to strong near-surface density stratification (Shetye et al., 1996; Gopalakrishna et al., 2002) and a shallow mixed layer, resulting in the formation of a barrier layer (Vinayachandran et al., 2002; Thadathil et al., 2007), which is a large area of heat trapping zone (below the mixed layer) conducive to cyclogenesis and intensification of tropical cyclones (Sengupta et al., 2008; Neetu et al., 2012; Balaguru et al.,

* Corresponding author at: Department of Mechanical Engineering, Massachusetts Institute of Technology, Cambridge, USA.
E-mail addresses: sudip@mit.edu (S. Jana), agangopadhya@umassd.edu (A. Gangopadhyay), pierrel@mit.edu (P.F.J. Lermusiaux), arunc@coral.iitkgp.ernet.in (A. Chakraborty), souravsil@iitbbs.ac.in (S. Sil), phaley@mit.edu (P.J. Haley).

https://doi.org/10.1016/j.jmarsys.2018.08.001
Received 21 February 2018; Received in revised form 1 August 2018; Accepted 2 August 2018
Available online 06 August 2018
0924-7963/

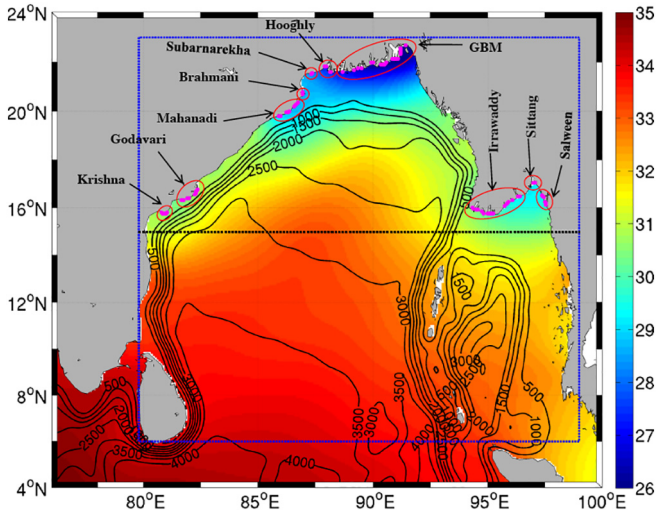

Fig. 1. The modeling domain overlaid with the climatological annual salinity in psu (color background). Contours represent the model bathymetry values in meters. Dotted blue lines represent the boundary of the domain of analysis. Magenta points along the coastal boundary are the locations of the point sources for river input. The black dotted line along 15°N demarcates the stratification analysis domains for northern and southern Bay of Bengal. (For interpretation of the references to color in this figure legend, the reader is referred to the web version of this article.)

2012; Chowdary et al., 2016; Lucas et al., 2016; Mahadevan et al., 2016; Sengupta et al., 2016; Seo et al., 2009 and Wilson and Riser, 2016). While the wind is favorable for the turbulent vertical mixing, the presence of strong stratification and a barrier layer inhibits the overturning convective mixing even when the surface water is cooler than the subsurface, resulting in temperature inversion (Thadathil et al., 2002). Moreover, both winds and stratification experience large spatiotemporal variabilities. Therefore, the complex interplay among the spatiotemporal variabilities in the wind and freshwater-induced stratification and barrier layer complicates the oceanography of this region. It is thus important to understand the sensitivity of the circulation and water-mass distribution of the BoB to wind and river forcing.

The main purpose of the present study is to investigate the sensitivity of high-resolution model simulations to different wind and river input setups. Two different wind-forcings – Comprehensive Ocean-Atmosphere Data Set (COADS) and Quick Scatterometer (QuikSCAT) were chosen because of their relative strengths. Two different river input salinity conditions, estuarine seasonal salinity and zero salinity, were chosen to induce appreciable changes in the resulting circulation and bracket the possible ocean responses. These choices yielded a set of four simulations that allow the individual and combined effects of winds (strong vs. weak) and river salinity inputs (fresh vs. saline) to be investigated and contrasted.

A number of modeling (Vinayachandran and Kurian, 2007; Seo et al., 2009; Sharma et al., 2010; Durand et al., 2011; Akhil et al., 2014; Rahaman et al., 2014; Benshila et al., 2014; Jana et al., 2015; Behara and Vinayachandran, 2016 and references therein) and observational studies (Pant et al., 2015; Chowdary et al., 2016; Lucas et al., 2016; Mahadevan et al., 2016; Sengupta et al., 2016) investigated upper-ocean salinity variability and its impact on both oceanic and atmospheric processes. Model simulations over the BoB without data assimilation or relaxation of surface salinity to climatology often suffer from positive salinity biases. Jensen et al. (2016) investigated the exchange of salinity between the Indian Ocean and the BoB using the Hybrid Coordinate Ocean Model (HYCOM) (forced by interannual winds) and a nested Regional Ocean Modeling System (ROMS) (forced by daily climatology) and concluded that knowledge of river input of fresh water is critical for modeling BoB surface salinities correctly.

A major source of limitation is the representation/parameterization of the freshwater inputs in the model. While the representation of precipitation in the model is relatively straightforward, the accurate representation of the river input in the model is still a big challenge to the ocean modeling community. Indeed, several modeling studies (Han and McCreary, 2001; Seo et al., 2009; Jana et al., 2015) showed that the river water plays the dominant role in modulating the surface salinity in the BoB. Different modeling studies parameterize the river inflow in different ways, e.g., as an open boundary condition (Chamarthi et al., 2008); as surface freshwater flux (Howden and Murtugudde, 2001; de Boyer Montégut et al., 2007); by distributing discharge over several model grids near the river mouth (Vinayachandran and Kurian, 2007), by using a coupled coastal-bay estuarine model (Rao et al., 2007), or as volume transport across the coastal boundary in terms of point source (Han and McCreary, 2001; Jana et al., 2015). Using a 1/12°-resolution ROMS configuration, Jana et al. (2015) studied the river impact on the Bay by incorporating the river input into the model in terms of point sources. The point sources were distributed along the model coastline where the inflow maintains an observation-based seasonal cycle of salinity (Fig. 4 of Jana et al., 2015). In the present study, in addition to the simulations with estuarine-like seasonal salinity river input, another set of simulations was conducted with purely fresh (i.e., zero salinity) river input to make a comparative assessment of the two river input representations.

The wind is one of the main driving forces of the BoB circulation. Moreover, the wind-driven turbulent mixing modulates the thermohaline and nutrient structure of the upper layers. The seasonally reversing wind results in the seasonal reversal of the boundary currents, both the springtime Western Boundary Current (WBC; Shankar et al., 1996, 2002; Durand et al., 2009; Gangopadhyay et al., 2013) and the autumnal East India Coastal Current (EICC; Cutler and Swallow, 1984; Shetye et al., 1991a; Suryanarayana et al., 1993). The southwest monsoon wind generates an eastward Ekman drift in a major part of the domain, and an upwelling along the Indian east coast brings subsurface nutrients to the surface. Prasanna Kumar et al. (2002) suggested that restricted vertical mixing due to the strongly stratified surface layers and comparatively weaker wind results in a BoB that is less productive than the Arabian Sea. Therefore, it is important to understand the sensitivity of the BoB to the different wind conditions.

Sensitivity studies in regional ocean basins using high-resolution models and wind products at different scales are a continuing research area. Chen et al. (1999) carried out a detailed sensitivity of the tropical Pacific to varying temporal and spatial resolution of winds. They found that monthly-averaged wind forcing helped increase the mean sea surface temperature (SST) compared to daily forcing by reducing the energy input for vertical turbulent mixing. Hogan and Hurlburt (2005) used monthly climatologies from seven different wind products (observed and reanalyzed) to force a 1.5-layer reduced gravity model of the Japan/East Sea, with varying degrees of success in resolving regional circulation for different products. Metzger (2003) studied the sensitivity of the circulation over the South China Sea (SCS) using a 6-layer Navy Layered Ocean Model (NLOM) and monthly mean climatologies using the Hellerman and Rosenstein (1983, hereafter HR), ECMWF (European Centre for Medium-Range Weather Forecasts) and NCEP (National Centers for Environmental Prediction) products. Hong and Wang (2008) conducted a no-wind vs. wind sensitivity study with monthly HR climatology and concluded that seasonal variability in the SCS is primarily wind-driven. Jensen (2011) studied the bifurcation of the Pacific North Equatorial Current to different monthly climatological winds from FSU (Florida State University), HR, and QuikSCAT. Kersale et al. (2011) performed a sensitivity study of the generation of mesoscale eddies around Hawaii using monthly climatological fields from COADS (weak) and QuikSCAT (strong) winds. Recently, Srivastava et al. (2016) carried out a set of 10-km-resolution BoB simulations using the MIT General Circulation Model (MITgcm) and obtained very similar circulation fields when forced by the coarser NCEP reanalysis winds in

comparison to when forced by blended 6-hourly high-resolution sea-wind products during 1998–2014.

Therefore, it is our goal to present sensitivity studies where the strength of the wind stress (weak vs, strong) is the key difference for wind forcing and where the salinity specification (seasonal salinity cycle vs. zero salinity imposition, with the same inflow) at the river point sources is the difference for the river forcing. The paper is organized as follows. Section 2 describes the modeling system setup and the four numerical experiments carried out in this study. Section 3 presents a large-scale statistical validation of the simulated fields by comparing the model-simulated annual mean and standard deviation of surface temperature and salinity, and sea surface height, mixed layer depth and mean thermocline depth against their corresponding climatological fields. Section 4 presents the sensitivity results for the surface circulation, temperature, salinity, eddy variability, stratification, barrier layer, freshwater plume and coastal upwelling. Section 5 highlights the main novel findings.

2. Model and methodology

2.1. Model setup

The modeling system setup is based on the study by Jana et al. (2015), which uses the Regional Ocean Modeling System (ROMS) (Haidvogel et al., 2000; Shchepetkin and McWilliams, 2003, 2005; Penven et al., 2006). The simulation domain (Fig. 1) extends from 76°E to 100°E and from 4°N to 24°N, with a uniform horizontal resolution of 1/12° (~9 km) and 32 terrain-following vertical layers. Vertical resolution was enhanced towards the surface by defining the s-coordinate surface and bottom stretching parameters as $\theta_S = 7.0$ and $\theta_B = 0.1$, respectively. In this configuration, high vertical resolution with < 1 m surface layers was realized near the surface, which helped in analyzing the near-surface processes with more confidence. These processes include the generation and propagation of freshwater plumes, which lead to formation of shallow mixed layer, strong near-surface density stratification and barrier layers. The model bathymetry field was extracted from the 2-min etopo2 (Smith and Sandwell, 1997) topography data. The model domain has open boundaries in the west, south, and east. On the open boundaries, we used the radiation condition (Orlanski, 1976; Marchesiello et al., 2001), which determines whether the boundary is passive (outward propagation) or active (inward propagation). The radiation condition allows the passage of information from the inner solution through the boundary when the boundary is passive; however, the solution is strongly nudged towards the specified lateral boundary condition when the boundary is active. This is analogous to the provided-Orlanski conditions (Haley and Lermusiaux, 2010; Haley et al., 2015). The model uses the double exponential parameterization of Paulson and Simpson (1977) for the solar irradiance penetration into the water column. The K-profile parameterization (KPP) scheme (Large et al., 1994) parameterizes the subgrid-scale vertical mixing processes in the interior and planetary boundary layers. Sponge layers of 100 km width were used near the open boundaries, where the maximum viscosity was set to 800 $m^2 s^{-1}$. Because of the implicit diffusion in the 3rd order upstream-biased advection scheme, the explicit lateral viscosity was null throughout the domain, except in the sponge layer. The physical and numerical parameters of the simulations shown are given in Table 1.

Climatological tracer and baroclinic geostrophic velocity fields (considering 1000 m as the depth of no motion) in the boundary condition were obtained from the 0.25° WOA01 (World Ocean Atlas 2001) monthly climatology (Boyer et al., 2005). The model was initialized from rest with tracer fields obtained from January values of WOA01. Monthly climatological forcing fields include: (i) shortwave and longwave radiations (averaged over 1983–2009) from the International Satellite Cloud Climatology Project (ISCCP; Zhang et al., 2004), which is hosted in the Objectively Analyzed Air-sea Fluxes (OAFlux) project (Yu and Weller, 2007; Yu et al., 2008) website; (ii) precipitation (averaged over 1949–2006) from CORE 2 (Coordinated Ocean Research Experiments version 2; Yeager and Large, 2008) datasets; and (iii) air temperature, air density and relative humidity from the 0.5° COADS (da Silva et al., 1994) monthly climatology. Two sets of wind forcings consisting of zonal and meridional wind velocities were obtained separately from monthly COADS and QuikSCAT climatologies. The latent and sensible heat fluxes, wind stresses and evaporation were calculated inside the model using the standard bulk formula of Fairall et al. (1996). Diurnal modulation of the shortwave radiation flux was imposed within the model. The forcing fields were mapped to the model horizontal grid using a bilinear interpolation. The river input provided in the model consisted of the climatological monthly discharges from the Krishna, Godavari, Mahanadi, Brahmani, Subarnarekha, Hooghly, Ganges, Brahmaputra, Meghna, Irrawaddy, Sittang and Salween Rivers. Monthly discharge data from the Global River Discharge Database (RivDIS v1.1) (Vorosmarty et al., 1998) and the Global Runoff Data Centre (GRDC) (Fekete et al., 2000) were used to obtain the climatological monthly mean discharges for these rivers except Hooghly, Meghna and Salween. Due to the unavailability of discharge data for the Hooghly, Meghna and Salween, we constructed their discharges using available observational studies: Sadhuram et al. (2005) and Rahaman et al. (2012) for Hooghly; Community Flood Information System (CFIS) report (Riverside Technology, Inc., 2008) for Meghna; and Syvitski et al. (2005) for Salween. The seasonal cycles of discharges for all the rivers are presented in Fig. 2 of Jana et al. (2015).

River inflows were prescribed in the model across the model coastal boundary in terms of a set of point sources. The discharge of each river was equally distributed along all its corresponding point sources. The point sources were distributed along the model coastline in such a way that the flow distribution of a river in the model approximately follows its realistic (geographic) flow distribution. The inflow amplitudes at each point source were vertically distributed in such a way that the flow velocity decreases with depth following a prescribed decay function. A detailed description of seasonal river input and its distribution in the model, and construction of the seasonal salinity cycles at the point sources, were presented in Jana et al. (2015). In this study, we used the constructed seasonal cycle as well the zero salinity for the river input for two sets of experiments. In all the simulations, the temperature of the inflow at each point source was set to the nearest WOA01 monthly climatological value. The detailed effects of river water temperatures on the BoB have not been considered here. In this work, we focused on the sensitivity of winds and salinity of rivers only. However, the sensitivity to the river temperatures should be investigated in the future.

The COADS and QuikSCAT wind products are the two widely used wind forcings for ocean models. The 0.5° × 0.5° COADS wind product is based on different in situ surface observations during 1945–1989,

Table 1
Dynamical model parameters.

Numerical parameters	
Domain	4–24°N, 76–100°E
Spatial resolution	1/12° (~9 km)
Vertical resolution	32 levels, s-coordinate
Physical parameters	
Time step for 3-D equation (dt)	600 s
Number of 2-D time steps within each 3-D step (ndtfast)	60
s-coordinate surface control parameter (θ_S)	7.0
s-coordinate bottom control parameter (θ_B)	0.1
Mean density	1025 kgm^{-3}
Linear bottom drag coefficient	3×10^{-4} ms^{-1}
Side wall boundary condition	1(free slip)
Sponge layer	100 km wide with maximum viscosity 800 $m^2 s^{-1}$

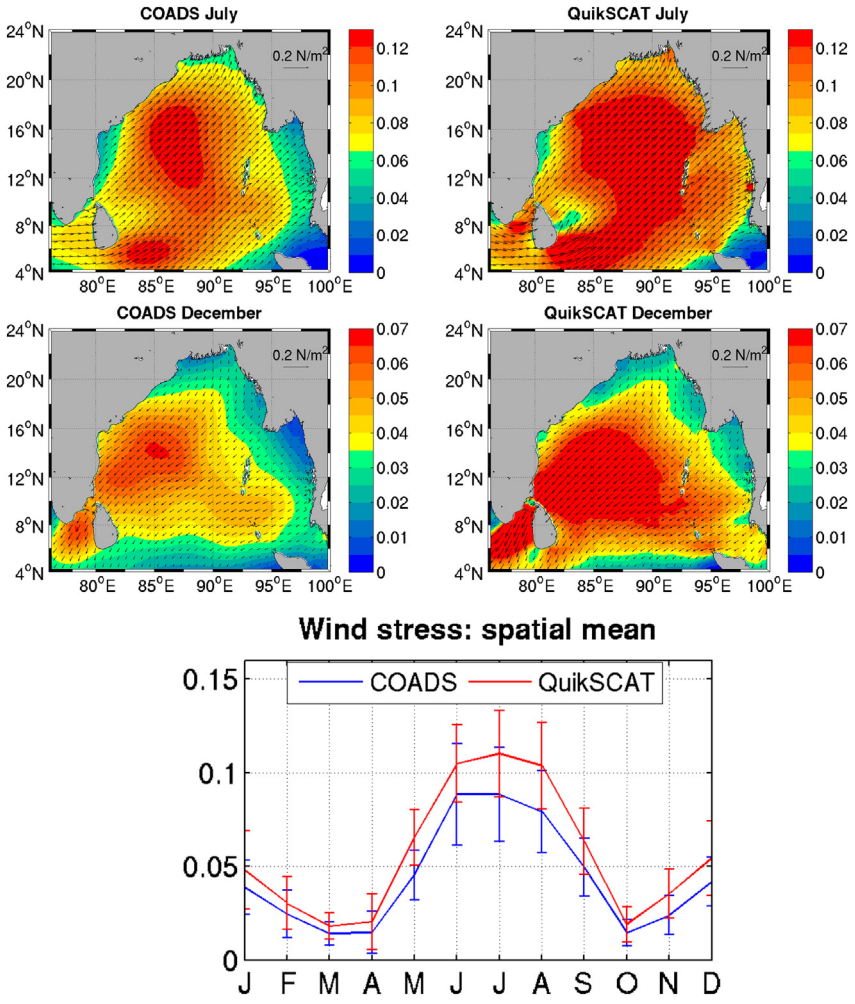

Fig. 2. Comparison of the weak and strong wind fields used for sensitivity studies. The panels in the top two rows show the wind stress vectors overlaid with corresponding magnitude for the weaker wind (COADS) on the left and stronger wind (QuikSCAT) on the right for July, representing the southwest monsoon period and for December, representing northeast monsoon period. Note the seasonal reversal of the wind direction. The fifth panel in the bottom row shows the seasonal cycle of the domain-averaged wind stress magnitude ($N\,m^{-2}$) from weaker COADS (blue line) and stronger QuikSCAT (red line). Note the difference between their strengths is accentuated during the summer. Bars on the lines represent the spatial standard deviation. (For interpretation of the references to color in this figure legend, the reader is referred to the web version of this article.)

whereas the $0.25^{\circ} \times 0.25^{\circ}$ QuikSCAT wind is the satellite-derived neutral winds. The monthly mean climatology of QuikSCAT winds was obtained by averaging the daily fields during September 1999–August 2007. The wind fields differ in strength month-by-month as shown by comparing the July and December wind stresses, representing the southwest and northeast monsoon periods, in the first four panels of Fig. 2(a, b, c, d). Fig. 2e captures the basin-wide average view, which shows that wind stress from the QuikSCAT wind is about 10–20% stronger than that of the COADS winds, with monsoon time (JJA) showing the largest difference. The weakness of the COADS winds can possibly be attributed to the large gaps between major shipping routes, which prevented the production of high-resolution gridded wind fields with high quality from only surface (volunteer ships of opportunity, buoys, dedicated surveys, etc.) observations (Risien and Chelton, 2008). The basin-wide average wind stress difference ranges from 0.001 to $0.02\,N\,m^{-2}$ (Fig. 2e), which is almost an order of magnitude higher than that corresponding to the uncertainty of about $1.5\,m\,s^{-1}$ for most of the available wind speed data in the Bay of Bengal (Satheesan et al., 2007; Praveen Kumar et al., 2013). The consistency in the difference in strength of the winds throughout the year is very useful to interpret the response of the upper ocean to the varying strength of the winds. As mentioned earlier, such monthly climatological winds were used in studies of other ocean regions (Hong and Wang, 2008; Hogan and Hurlburt, 2005; Jensen, 2011; Kersale et al., 2011; Metzger, 2003) to investigate the sensitivity of the upper ocean to different wind forcings.

2.2. Numerical experiments

A set of four modeling experiments are presented based on the different combinations of the two wind forcings (weaker COADS and stronger QuikSCAT) and two river input representations (estuarine-like river inflow with seasonally varying salinity and purely fresh river inflow with zero salinity). All the simulations utilize the same initial, boundary and forcing conditions except for the winds and river inputs. Table 2 summarizes these runs and designates each with a unique run-name, which is followed throughout the manuscript. These are: CRS for COADS-forced River run with seasonal salinity input; QRS for QuikSCAT-forced River run with seasonal salinity input; CRZ for COADS-forced River run with zero salinity; and QRZ for QuikSCAT-forced River run with zero salinity. Each of the simulations was run for 15 years. We note that different basins reach dynamical equilibrium

Table 2
Summary of the main sensitivity simulation experiments.

Sensitivity experiment	Wind forcing (monthly climatology)	River input salinity parameterization
CRS	Weaker Winds (COADS) - C	River input with *seasonal salinity* - S
QRS	Stronger Winds (QuikSCAT) - Q	(i.e. Weaker Buoyancy)
CRZ	Weaker Winds (COADS) - C	River input with *zero salinity* - Z
QRZ	Stronger Winds (QuikSCAT) - Q	(i.e. Stronger Buoyancy)

depending on the time required for the first and second baroclinic mode Rossby waves to reach the western boundary from the eastern boundary (Kantha and Clayson, 2000). Earlier long-term simulations in the Bay of Bengal and Arabian Sea have shown spin-up periods of a few months to a few years (Jensen, 2011; Benshila et al., 2014) due to the regional geography and smaller zonal width than either Atlantic or Pacific basin. Our simulations reached dynamic equilibrium after 5–7 years in a domain-average sense between the mass and momentum fields (see Fig. 5 of Jana et al., 2015, for the adjustment evolution). Therefore, we have treated the first ten years (years 1–10) of the simulations as spin-up and the last five years (years 11–15) for the sensitivity analysis. We have averaged the last five years of simulated fields to avoid the model internal variability and provide a best estimate of a statistically invariant, month-by-month mean state evolution of the ocean fields. This averaged field evolving over a full canonical year is commonly referred to as a model climatology. It is then compared and contrasted with the data-based climatologies (NIOA temperature and salinity, AVISO SSH and OSCAR surface currents), with an emphasis on the main features of the BoB. This is a typical approach for the validation and comparison of model-derived fields against data-based climatologies.

3. Statistical validation of the simulations

In this section, we present a statistical validation of the simulations against the available climatology and other datasets through the computation of mean, standard deviation, bias, root mean square difference (RMSD), correlation coefficient, and skill. The bias is defined as the difference between domain-averaged annual means from the simulated versus climatological fields (i.e. simulation minus climatology). Performances of all the simulations are also evaluated using a skill score (Taylor, 2001) given by the following formula:

$$S = \frac{4(1+R)}{\left(\sigma + \frac{1}{\sigma}\right)^2 (1+R_0)}$$

where σ is the normalized standard deviation, R is the correlation coefficient, and R_0 is the maximum correlation attainable (considered as 0.99 following Schmidt and Gangopadhyay, 2013). The model-simulated SST, sea surface salinity (SSS), mixed layer depth (MLD), and D23 (depth of the 23 °C isotherm) are compared with those from the North Indian Ocean Atlas (NIOA; Chatterjee et al., 2012); climatology and model-simulated SSH are compared with the altimeter-derived SSH (gridded map of Absolute Dynamic Topography – ADT) from AVISO. The monthly and annual climatologies of AVISO SSH were obtained by averaging the daily fields during 1993–2013. The MLD is defined as the depth at which the density is greater than the surface density by a quantity equivalent to a 1.0 °C temperature drop (Wyrtki, 1971; Thadathil et al., 2007; Seo et al., 2009). The D23 represents the depth of the 23 °C isotherm as the proxy of the mean thermocline depth (Girishkumar et al., 2013).

3.1. Basin-wide statistical validation of annual fields

Fig. 3 presents the annual mean fields of SST, SSS, SSH, MLD, and D23 obtained from climatology (1st column) and the four model simulations (2nd-5th columns) for CRS, QRS, CRZ, and QRZ. Note that, for consistency, the simulated fields are bin-averaged over the climatological grid. The spatial maps of the biases in the simulated fields with respect to their observed climatological values are also shown in Fig. 3. Domain-averaged values of these biases are presented in Table 3. The simulated SST fields (Fig. 3, 1st row) are slightly warmer than the climatology in all the simulations; however, the spatial distribution of the SST in all the simulations compares reasonably well with the climatology, showing relatively lower SST in the northern part and warmer SST in the southern part. This warm biases are reduced (by ~0.2 °C) when the simulations (QRS and QRZ) are forced by QuikSCAT wind (see Table 3, SST column). Note that the simulated SST fields in Fig. 3 are shown after removing their corresponding biases to make the visual comparison comprehensible with the same colorbar.

The warm bias in SST for all simulations is attributable to: (i) initial adjustment of the climatological temperature field to atmospheric fluxes in the first few weeks of simulation, as indicated by Jana et al. (2015), and (ii) the use of weaker climatological winds (both COADS and QuikSCAT-derived climatology are weaker than real atmospheric winds) resulting in weak vertical mixing, hence trapping more heat in the near-surface layers raising the surface temperature. The SSS bias for the CRZ run is near zero (Table 3), and all other simulations have a salt bias. From a sensitivity perspective, the stronger winds resulted in stronger mixing, and both the QRZ and QRS simulations raised salinity at the surface by mixing the higher subsurface salinity with lower surface salinity. At the same time, all the simulations were positively biased from climatological SSS due to less spreading of the freshwater plume in the winter months, as will be shown later. In general, higher SSS biases in the simulations resulted in a deeper MLD compared to climatological observations due to either or both of the above reasons (less freshwater spreading and/or mixing).

The model-simulated SSS fields are in general agreement with the climatology in reproducing the north-south high spatial contrast with a positive gradient from north to south (Fig. 3, 2nd row). The extreme freshness at the northern end of the Bay due to large freshwater input from the Ganges-Brahmaputra-Meghna (GBM) and Hooghly rivers is well-captured in the simulations. Another low-salinity patch at the head of the Andaman Sea due to the fresh water from the Irrawaddy, Sittang, and Salween rivers is also captured reasonably; however, the values are slightly higher in the simulated SSSs. The higher salinity in the south-western Bay has a signature similar to that of the E-P field in this region (not shown) and could possibly contribute significantly in addition to possible excess transport from the Arabian Sea. The surface salinity bias is greater in the stronger-wind simulations (QRS and QRZ) than in the weaker-wind simulations (CRS and CRZ; see Table 3, SSS column). Except for the bias differences, the correlation and skill for the magnitude and spatial distribution of surface salinity for all four simulations compare reasonably with one another. It is interesting to note that weak winds help in realizing surface salinity simulations that are closer to climatology.

Fig. 3 (3rd column) and Table 3 (SSH column) compare the simulated SSHs (ROMS Zeta field) with the AVISO ADT (Absolute Dynamic Topography). It is important to note that the ROMS-simulated SSH (zeta) is not directly comparable with the AVISO Sea Level Anomaly (SLA). ROMS SSH is calculated with respect to a datum, z = 0, while AVISO SLA is measured with respect to the mean geoid and temporal mean currents (Mean Dynamic Topography, MDT) (Strub et al., 2015; Vic et al., 2014). Levin et al. (2018) recently explained that the ROMS sea level is effectively the ADT (MDT + SLA) of the AVISO fields, without the nondynamic geoid (Strub et al., 2015). Furthermore, the ROMS zeta field ranges from −0.2 to 0.4 m, which differs considerably from the AVISO ADT field (range between 0.6 and 1.5 m) over the year. Therefore, AVISO ADT fields were compared (with ROMS zeta) after removing a temporal and spatial mean (annual mean and domain-averaged value) to make them approximately consistent with the reference level of the ROMS simulations (Manyilizu et al., 2014), which does not contain the larger-scale nondynamic geoid. In agreement with the observations, the simulated SSH is higher along the northern and eastern boundary and the central part of the BoB, while SSH is lower along the western boundary and in the southwest part the BoB. The SSH-ADT correlation (skill) significantly increased from 0.70 (0.81) to 0.84 (0.92) when weaker winds, instead of the stronger winds, were used for the seasonal salinity river input runs. For the zero salinity runs, similar increases ranged from 0.76 (0.80) to 0.86 (0.93). On the other hand, the impact of zero salinity increase the SSH correlation (skill) from 0.70 (0.81) to 0.76 (0.85) for the weaker-wind runs and from 0.84 (0.92) to 0.86 (0.93) for the stronger-wind runs. Therefore, while

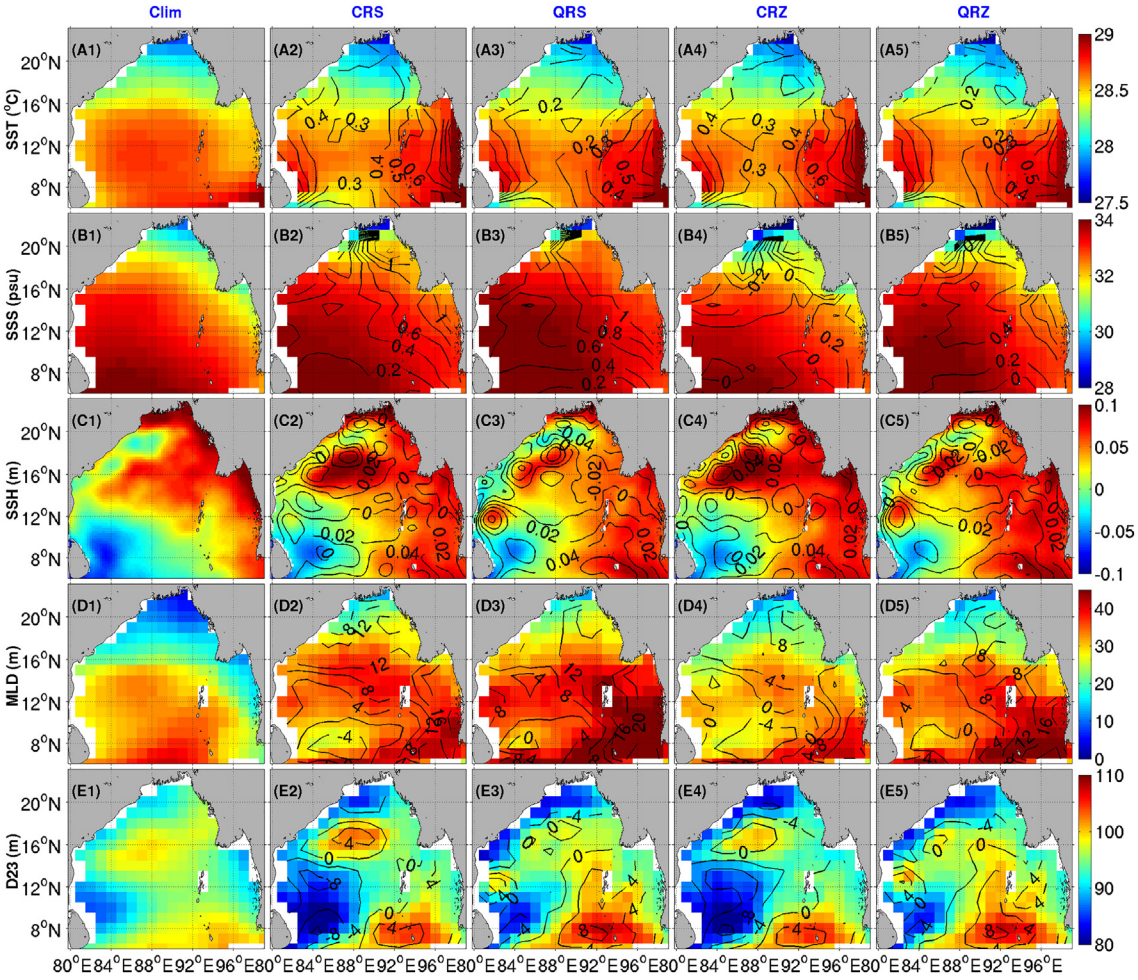

Fig. 3. Annual fields of SST (°C), SSS (psu), SSH (m), MLD (m), and D23 (m) are shown along five rows (from top to down) for the NIOA climatology (1st column) and from the CRS (2nd column), QRS (3rd column), CRZ (4th column) and QRZ (5th column) model simulations. To maintain the same color range, the simulated SSTs (top row) are presented after removing their respective biases (see Table 2). Simulated fields are binned averaged over the climatological grid. Contour lines represent biases. The AVISO field on Row 3, Column 1 is for the ADT from AVISO data, with its annual- and spatial-average subtracted to match the range of the ROMS zeta fields (Columns 2 through 5).

stronger winds reduced the skill by almost 0.10, increasing buoyancy boosted the skill marginally, in the range of 0.01 to 0.04.

The freshwater-induced shallow MLD in the northern BoB is reasonably reproduced in the simulations (Fig. 3, 4th row). As expected, the stronger wind forces a deeper MLD (by ~3–10 m over an annual cycle, domain averaged) in the simulations as compared to the weaker wind forcing. Quantitatively, stronger winds increased MLD correlation (skill) from 0.59 (0.70) to 0.66 (0.82) for the seasonal salinity runs and from 0.73 (0.79) to 0.77 (0.80) for the zero salinity runs. The fresher river inputs led to an increased correlation (skill) from 0.59 (0.70) to 0.73 (0.79) for the weaker-wind runs and from 0.66 (0.79) to 0.77 (0.89) for the stronger-wind runs. Hence, increasing buoyancy for fixed wind-forcing (either strong or weak) and strengthening winds for fixed buoyancy (at zero or seasonal salinity) had similar effects on MLD skill, namely, increased it individually by almost 10%. The simulated MLD has the smallest bias for CRZ and has maximum correlation for QRZ.

The deeper D23 in the central part of the BoB and shallower D23 near the boundaries are reasonably reproduced in the simulations (Fig. 3, 5th row). Simulated domain-averaged D23s are slightly (~3–5 m) shallower, with a correlation > 0.55 with climatology (Table 3). The standard deviation of the annual mean for the simulated D23 is generally higher than that of the climatology, which reduces the correlation and skill values for D23 simulations to the lowest among all five variables.

The effects of the different factors as per different simulations are graphically presented in the Taylor diagram (Fig. 4) and can be summarized as follows. The highest (lowest) correlations are obtained for SSS (D23). The impact of zero salinity in river input is clearly evident in moving the SSS and MLD (compare M2/M4 with M1/M3) towards climatology. The impact of the stronger winds is most evident in moving the MLD towards climatology in the direction of higher correlation. The temperature and D23 clusters are relatively tighter, indicating more direct linkage to wind or river forcing. On the other hand, SSH shows a more complex sensitivity to both winds and river input, evident in the large spread from H1 to H4.

3.2. Basin-wide statistical validation of seasonal variability

Fig. 5 compares the maps of the standard deviation of the annual mean for the SST, SSS, SSH, MLD, and D23 obtained from all four simulations against climatology. The standard deviation is computed from the 12 monthly-average values at every grid point to assess the seasonal variability of the parameter of interest. The simulated variabilities for the SST (row 1) and SSS (row 2) agree reasonably well with the corresponding climatological variabilities except in the northern end of the Bay, where the simulated SSS is slightly overestimated. Note that both the SST and SSS variability increase with zero salinity simulations (compare CRS/QRS to CRZ/QRZ). For SSH (Fig. 5, row 3), all

Table 3
Annual statistics of five main physical parameters for the four different numerical experiments.

		SST (°C)	SSS (psu)	SSH (m)	MLD (m)	D23 (m)
CRS	Bias	0.46	0.42	0.039	7.49	−1.67
	Std	0.28	0.87	0.037	5.71	6.33
	Correlation	0.81	0.94	0.84	0.59	0.79
	Skill	0.87	0.96	0.92	0.70	0.62
	RMSD	0.49	0.54	0.045	10.07	4.55
QRS	Bias	0.28	0.69	0.035	10.68	0.41
	Std	0.27	0.82	0.033	7.24	5.83
	Correlation	0.85	0.92	0.70	0.66	0.73
	Skill	0.90	0.93	0.81	0.82	0.65
	RMSD	0.32	0.80	0.046	12.48	4.09
CRZ	Bias	0.45	−0.03	0.045	3.29	−2.72
	Std	0.29	1.17	0.040	6.06	6.21
	Correlation	0.83	0.93	0.86	0.73	0.77
	Skill	0.87	0.94	0.93	0.79	0.62
	RMSD	0.48	0.44	0.050	6.55	5.02
QRZ	Bias	0.27	0.30	0.043	6.82	0.43
	Std	0.29	1.11	0.034	7.78	5.64
	Correlation	0.88	0.94	0.76	0.77	0.74
	Skill	0.89	0.96	0.85	0.89	0.68
	RMSD	0.31	0.50	0.051	8.72	3.90

**Standard deviation (Std) for annual climatological fields: 0.23 °C (SST), 0.98 psu (SSS), 0.042 m (SSH), 8.29 m (MLD), 3.37 m (D23). Note that the correlation for SSH is between AVISO ADT and ROMS zeta field. While computing the rmsd for SSH, the annual- and spatial-average of ADT was removed so that the range of sea surface height variability compares with that of ROMS zeta field.

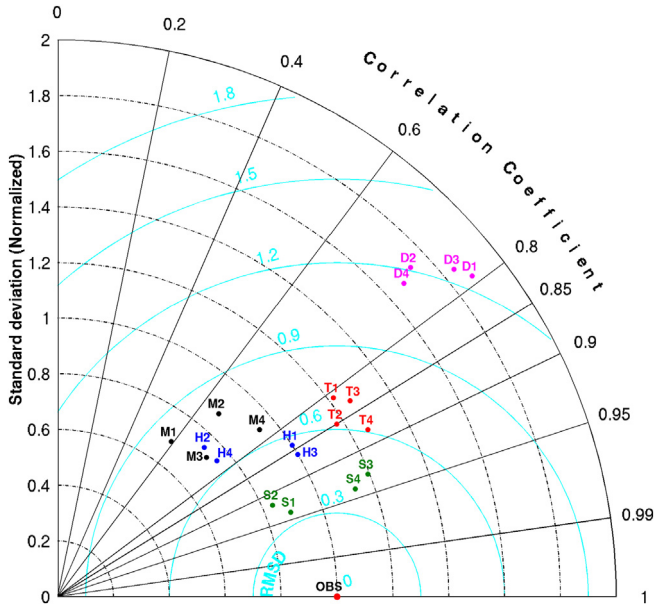

Fig. 4. Taylor diagram showing the model skill (correlation, normalized standard deviation and centered RMSD) to simulate the climatological annual SST (T1, T2, T3, T4), SSS (S1, S2, S3, S4), SSH (H1, H2, H3, H4), MLD (M1, M2, M3, M4) and D23 (D1, D2, D3, D4). Suffixes 1, 2, 3 and 4 indicate fields from CRS, QRS, CRZ and QRZ respectively.

four simulations show higher eddy activity associated with both the boundary currents than does the climatology in the western Bay. The pattern of the simulated structure of the SSH variability along the northwestern BoB is similar to that observed in the AVISO field; however, the regional extent of simulated variability is underestimated. The simulated variability for MLD is generally greater than the climatology in the northern Bay (Fig. 5, 4th row). This is due to the greater range of MLD in the simulations during the winter (see Fig. 14 of Jana et al., 2015, for MLD seasonal cycle). The overall pattern of simulated D23 compares reasonably with that of climatology (higher along the western boundary and lower over the rest of the domain), which is also consistent with the SSH variability (Fig. 5, row 3). Note that the QRZ simulation consistently yielded closer domain-wide agreement with the climatology for SSH, MLD and D23, a result that is probably related to its capability of resolving subsurface variability.

Note that the spatial distribution of all these parameters, except the SST, is highly impacted by the complex circulation and eddy activities. Thus, the performance of high-resolution eddy-resolving models in reproducing the seasonality of these parameters becomes heterogeneous in space.

4. Sensitivity results

In this section, we describe how the different wind forcings and river salinity conditions of the four simulations affect the results of these simulations. Specifically, we study the sensitivity to the wind and river input salinity of the surface circulation features, basin-wide dynamic tracer and eddy kinetic energy (EKE) fields, vertical water mass structures, freshwater plume dispersion, and coastal upwelling.

4.1. Sensitivity of the surface circulation

Fig. 6 compares the model-simulated upper ocean circulation during March–April, July–August, and October–November for all four simulations with the fields from the Ocean Surface Current Analysis in Real-time (OSCAR, 1st row). The OSCAR fields are a composite of wind-derived Ekman drift (with a Stommel shear layer), altimeter-derived geostrophic currents, and the SST-derived buoyancy gradient component over the upper 30 m of the water column. They are available from https://podaac.jpl.nasa.gov/dataset/OSCAR_L4_OC_third-deg at 1/3° resolution and 5-day interval. Simulated currents were depth-integrated in the upper 30 m, and the equivalent OSCAR-like upper ocean currents were computed by averaging over that depth. Circulations from all four simulations are shown in rows 2, 3, 4, and 5, respectively. The March–April circulation includes the mature phase of the WBC, the July–August circulation captures the impact of southwest monsoon winds and enhanced river inflow, and the October–November circulation depicts the mature phase of the EICC.

The sensitivity of the springtime WBC to winds and river input is best described through the left column of Fig. 6. The 5-year average signature of the WBC (Fig. 6, left column) is that of a continuous flow from 11°N to 18°N in CRS and then separating at around 18.5°N as observed by many investigators (e.g., Legeckis, 1987; Durand et al., 2008; Gangopadhyay et al., 2013). Stronger winds generate a stronger WBC (compare QRS/QRZ to CRS/CRZ) because of the integrated wind-curl effect during winter.

The sensitivity of the monsoonal circulation to winds and rivers is illustrated by the July–August fields (Fig. 6, middle column). During this period, a subbasin-scale gyre, called the North Bay Cyclonic Gyre (NBCG: Jana et al., 2015), forms at the head of the BoB (Varkey et al., 1996; Shetye, 1993; Haugen et al., 2002; Vinayachandran and Kurian, 2007; Jana, 2014). This gyre plays an important role in controlling the spreading of the GBM freshwater plume (Jana et al., 2015). The southern arm of this gyre, termed the North Bay Monsoon Current (NBMC: Vinayachandran and Kurian, 2007), separates the fresh water of the north from the saltier water of the south. Although the NBCG is reasonably well simulated in all four simulations, its structure is most pronounced for CRZ and CRS; the eastern edge of the NBCG in QRS is slightly disorganized.

An interesting feature in all four simulations is the presence of an anticyclonic eddy centered near 12°N, 82°E, adjacent to the western boundary just north of Sri Lanka. This eddy is stronger in the stronger-wind simulations (QRS and QRZ). Some evidence of this eddy is shown in the simulations and altimeter-derived geostrophic velocity field presented by Vinayachandran and Kurian (2007) (see their Fig. 12c–d).

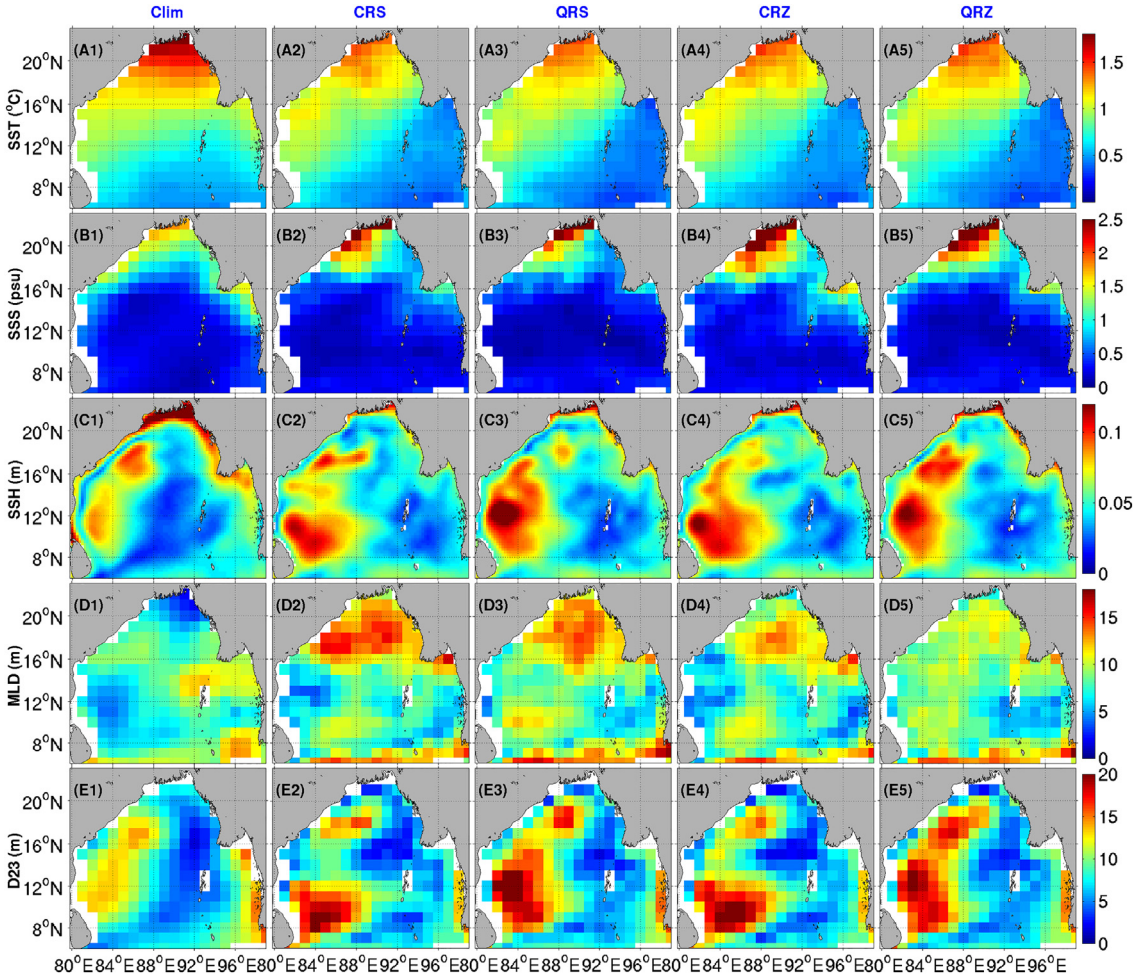

Fig. 5. Comparison of the standard deviation of the annual mean between the NIOA climatology (1st column) and the four simulations (2nd–5th columns) for SST (1st row: A1–A5), SSS (2nd row: B1–B5), SSH (3rd row: C1–C5), MLD (4th row: D1–D5), and D23 (5th row: E1–E5). Model simulated fields are binned averaged over their corresponding climatological grid.

All four simulations reasonably capture the eastward flow in the central Bay and the southwest monsoon current (SMC) along the southern boundary, which are in agreement with other model simulations (Vinayachandran and Kurian, 2007; Benshila et al., 2014); however, OSCAR fields do not show this on average. The ROMS-simulated currents are stronger and more eddy-dominated than OSCAR fields because of differences in their resolution (1/12° vs. 1/3°) and temporal averaging period (5 years vs. 21 years). Several observational (Gangopadhyay et al., 2013, and references therein) and model simulations (Vinayachandran and Kurian, 2007, and references therein) indicated the existence of such strong eddies in the BoB.

The mature phase of the southward EICC during October–November is presented in the right column of Fig. 6. Compared to the continuous path of the EICC in OSCAR, all four simulations show somewhat weaker and narrower current along the east coast. In addition, we note a westward flow in the west-central Bay that joins the EICC at around 14–15°N, which is supported by other model simulations and observations (Vinayachandran and Kurian, 2007, and references therein).

4.2. Sensitivity of the basin-wide temperature, salinity, and EKE

We now investigate the sensitivity of model temperature, salinity, and EKE to wind bias and/or river/estuary freshness variations (Fig. 7). The annual cycle of surface-averaged temperature (Fig. 7a) shows negligible sensitivity to changes in the river salinity; however, the stronger winds lower the average temperature by almost 0.25 °C throughout the year compared to weaker-wind runs. This indicates the dominant role of the wind in determining the BoB SST variability. The volume-averaged temperature (figure not shown) is lower (~0.01 °C) for both of the weaker-wind runs (CRS and CRZ) than for stronger-wind runs (QRS and QRZ). Although this difference is not significant at the 95% CI, the reason for such differences might be that the weaker winds do not mix the upper ocean deeply enough for the heat to penetrate below the mixed layer. Note that the fresher river input results in an even stronger near-surface stratification, which traps even more heat in the barrier layer to further lower the volume-averaged temperature (integrated over the full water column) for the CRZ run from that of the CRS run.

The sensitivity of the surface-average salinity to wind and river input salinity variation (Fig. 7b) is rather straightforward. Stronger wind enhances mixing, resulting in higher salinity at the surface. At the surface, this increase is about 0.4 psu for 0.1 N m^{-2} of increase in wind-stress magnitude. The zero-salinity imposition lowers the seasonal simulations by about 0.3–0.4 psu in winter-spring to about 0.5–0.6 psu in October. The volume-averaged salinity (figure not shown) amplitude follows similar behavior at a much smaller amplitude (~0.005 psu).

Next, we present the annual cycle of the surface EKE for four different runs (Fig. 7c). The EKE is calculated as $EKE = [u'^2 + v'^2]/2$, where u' and v' are the annual mean-removed zonal and meridional components of the velocity, respectively (Capotondi et al., 2009). The EKE shows a semi-annual periodicity with peaks in summer and winter and troughs in autumn and spring. Evidently, the EKE for both stronger-

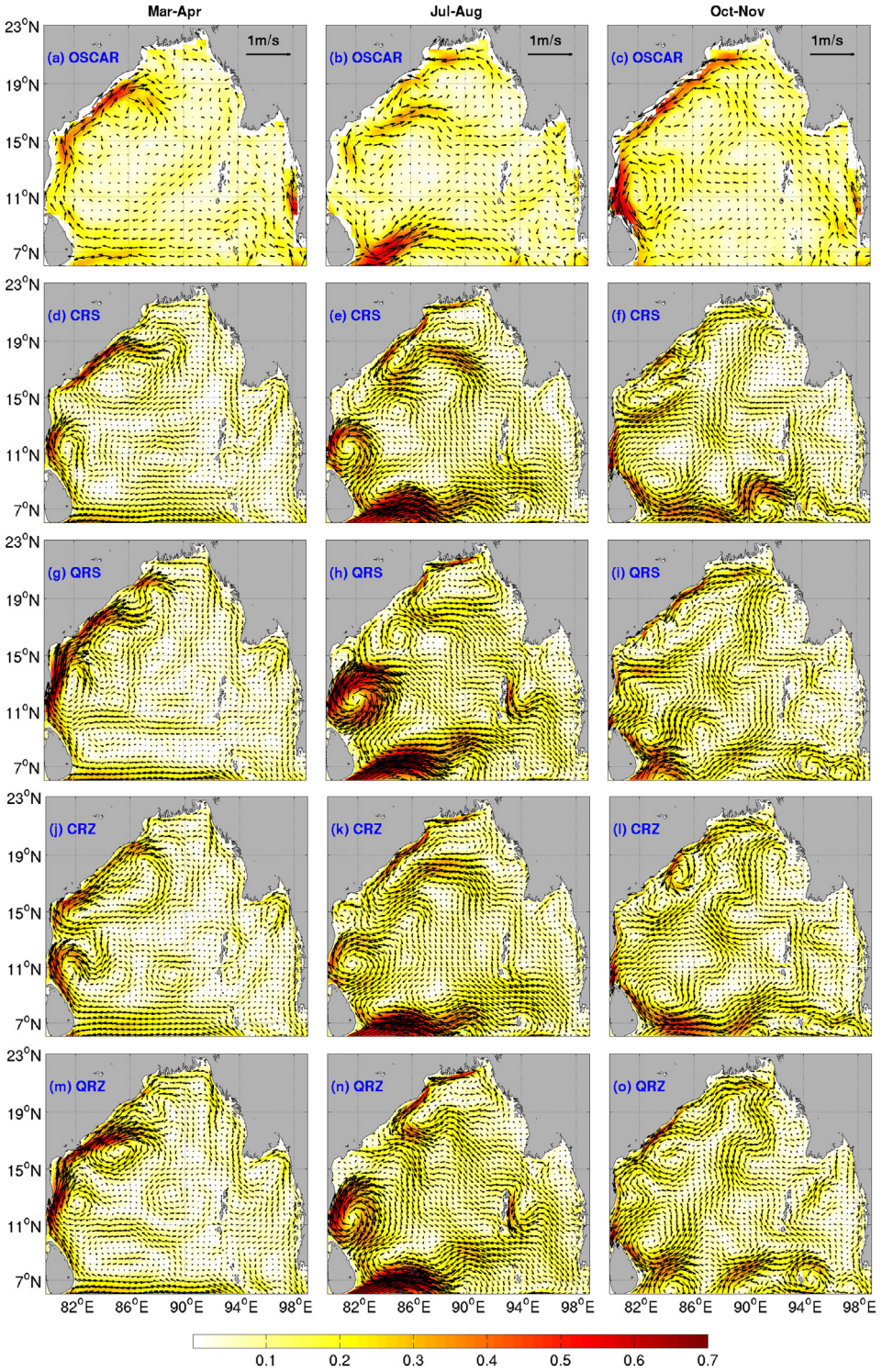

Fig. 6. Comparison of upper Ocean circulation for Mar-Apr (left column), Jul-Aug (middle column) and Oct-Nov (right column) between the OSCAR fields (top row) and four simulations in next four rows. Shaded background represents magnitude ($m\,s^{-1}$) of the velocity. The simulated upper ocean flow vectors were computed by depth-averaging the upper 30 m velocity fields as done for OSCAR.

wind runs (QRS and QRZ) are higher than their respective weaker-wind counterparts (CRS and CRZ) throughout the year (Fig. 7c), due largely to their individual strengths. The dominant wind-driven EKE annual cycle is modulated by the river input salinity choices as follows. Compare the annual EKE cycles (Fig. 7c) for fresher river condition (QRZ/CRZ) with their respective saline counterparts (QRS/CRS). The EKE peak for the fresher simulations during the summer monsoon is lower than for their respective seasonal salinity counterparts, while being higher during the periods of autumn EICC and transition to spring WBC. This indicates that while the eddy activity in the BoB is mostly forced by winds during the year, their seasonality is modulated by the river input in reducing (enhancing) the wind-induced impact during summer (winter) monsoon.

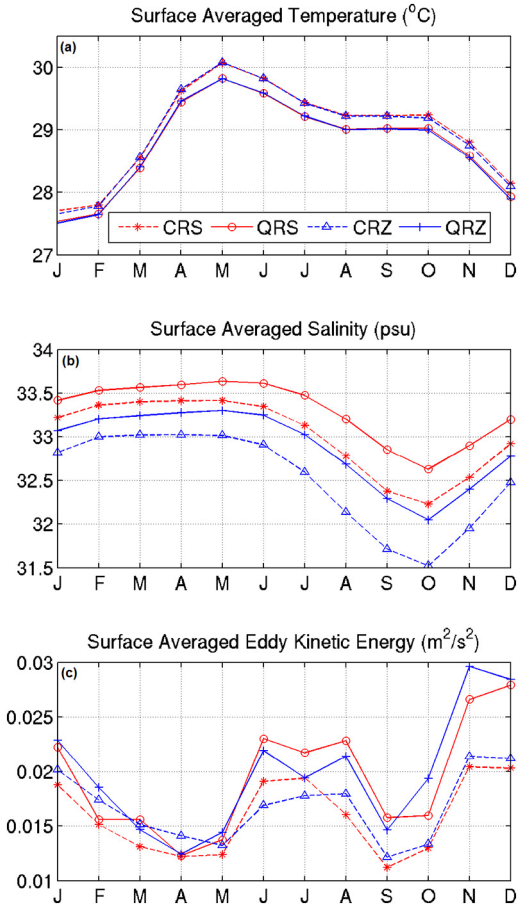

Fig. 7. Surface averaged temperature, salinity and eddy kinetic energy from all four simulations. Legends are same for all the panels, shown in the inset of the top-left panel. See text for details.

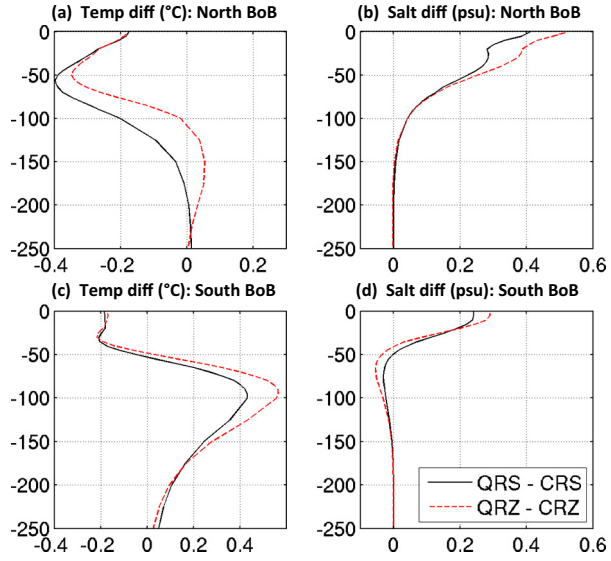

Fig. 8. Sensitivity to different wind forcing of the simulated temperature (°C) (left column) and salinity (psu) (right column) fields in the northern (top row) and southern BoB (bottom row). Difference (QuikSCAT – COADS) for the two buoyancy conditions (zero and seasonal salinity) are shown. Note that the effect of stronger winds (QuikSCAT) is felt (i) deeper for temperature than for salinity, and (ii) has different responses in the upper 200 m of the southern Bay than in the northern Bay. See text for details. (For interpretation of the references to color in this figure, the reader is referred to the web version of this article.)

4.3. Regional sensitivity of the vertical structures of water masses

The impact of the wind is reflected in different vertical distributions for temperature and salinity in the upper ocean, but down to similar depths in both the northern and southern Bay. Fig. 8 shows this impact in terms of differences in the vertical profiles of spatially averaged annual mean temperature and salinity between the weaker COADS and stronger QuikSCAT wind-forced simulations spatially over the northern and southern BoB. Note that the impacts on temperature and salinity differ significantly, not only in terms of vertical pattern, but also in their amplitudes between the northern and southern BoB. The stronger winds lead to an apparent cooling near the surface (< 50 m) in the southern BoB, accompanied by a subsurface warming (Fig. 8c). This thermal change is also accompanied by a parallel salinity increase in the upper layer (< 50 m) and decreasing salt below (50–150 m; see Fig. 8d). Clearly, both of these behaviors can be attributed to the stronger wind-induced enhanced mixing, which resulted in cooling (salting) near the surface and warming (freshening) below the surface mixed-layer. The warming of the subsurface layer between 50 and 150 m in the northern Bay (Fig. 8a – red dashed line) arises from an anomalous warming during February through May, the reasons for which remain unclear as of this writing.

Fig. 9(a, b, c) shows the resulting impact of winds and rivers on the upper layer stratification in the northern and southern BoB and over the full domain of the Bay. The stratification is represented by the static stability parameter ($E = -\frac{1}{\rho}\frac{\partial \rho}{\partial z} - \frac{g}{C^2}$, where ρ is the density at depth z, C is the speed of sound, and g is the gravitational acceleration), computed following Pond and Pickard (1983). The maximum impact of the reduced river salinity input occurs in the near-surface stratified layers of the northern BoB (Fig. 9a), where the near-surface (~10 m) peak of static stability reaches to about $15 \times 10^{-5}\,m^{-1}$ ($10 \times 10^{-5}\,m^{-1}$) for the COADS (QuikSCAT) run. The simulated stratification is very well resolved in the upper 20 m of the northern BoB due to higher vertical resolution near the surface adopted in the model. Note the high amplitude of the near-surface peak compared to the NIOA climatology peak at only $6 \times 10^{-5}\,m^{-1}$. This is due to the coarse vertical gridding of the climatology, which has its upper three layers at 0, 10 and 20 m. If the simulations were averaged vertically on the climatological grid, the static stability profiles from simulations would match those of the climatology very well. Note that the zero-salinity runs enhance the stratification of the southern BoB also down to 60 m; however, the near-surface maxima in averaged static stability profiles are absent in all the simulations for the southern BoB. This finding confirms the results of Jana et al. (2015), indicating that the major impact of river input is indeed restricted to the northern Bay (north of 15°N). Due to the enhanced vertical mixing because of the stronger QuikSCAT wind, the averaged stability is reduced above ~120 m (~80 m) in the northern (southern) BoB and is slightly enhanced below that.

4.4. Sensitivity of the EICC, freshwater plume dispersion and barrier layer

Next, we discuss the sensitivity of the EICC and of the freshwater plume dispersion to the river salinity for the period of July through December. In Fig. 10, we compare the SSS of the four simulations with NIOA climatologies. Following Jana et al. (2015), the 32.5-psu isohaline contour is designated as the demarcation of the boundary of the freshwater plume in the simulations and indicated in all panels of Fig. 10. The comparison results are as follows. First, the freshness of the core of the EICC (recognized by the $0.5\,m\,s^{-1}$ southward velocity along the coast) for QRZ is increased by about 4.0 psu from that of QRS, as is apparent at 15°N. Second, the EICC for the QRZ is stronger by about $0.05\,m\,s^{-1}$ than for the QRS flow (Fig. 6), indicating that the salinity contrast is a significant contributor to the formation and growth of the EICC. Third, the spread of the freshwater plume (marked by the 32.5 psu isohaline contour) is larger for the QRZ towards the central

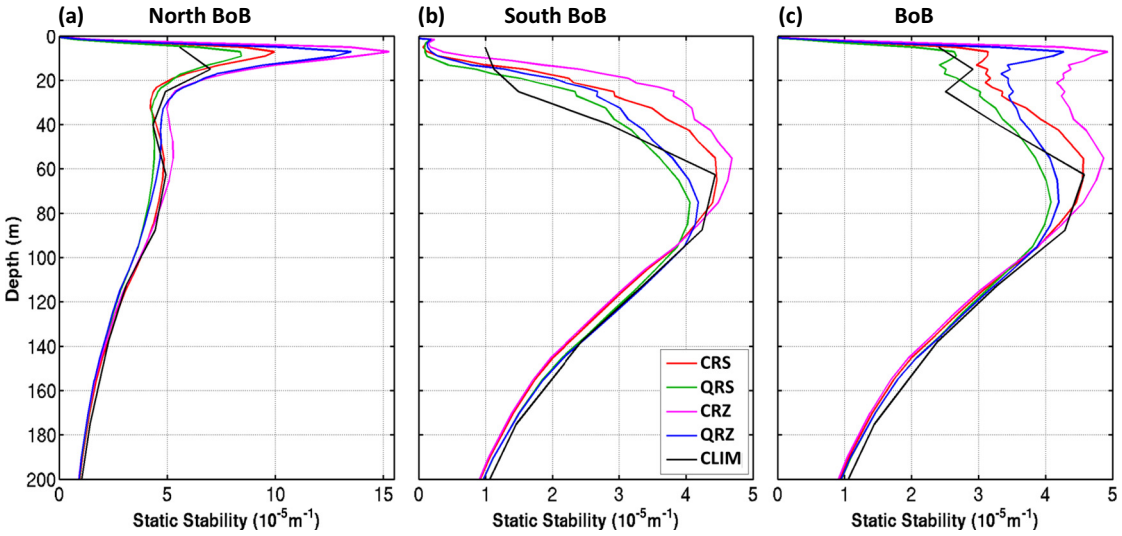

Fig. 9. Comparison of vertical profiles of mean static stability during July through October, averaged over the (a) northern BoB (north of 15°N), (b) southern BoB (south of 15°N) and (c) entire BoB, between climatology (NIOA), and the four simulations.

and eastern Bay. Finally, for QRZ, the EICC penetrates further south to 14°N (9°N) compared to 17°N (15°N) for the QRS during Oct (Nov), as is evident from the leading edge of the EICC coinciding with the 32.5-psu contour near the coast.

Fig. 11 presents the relative performance of the four runs in capturing the area, volume, and vertical extent of the plume. Three important inferences are drawn. First, the timing of reaching the maxima in volume and vertical extent generally lags the timing of the maximum surface spreading by about two months. The surface spreading matures in October, followed by the other two in December, as was reported by Jana et al. (2015). Second, with regards to sensitivity, the impact of winds (weak vs. strong) is felt almost uniformly throughout the year for surface spreading and is about 10% greater for the weaker COADS wind. Similarly, zero-salinity river input causes 10% (0.1%) more spreading (volume) over seasonal salinity input during most of the year, except for being a bit higher (15%; 0.15%) during the post-monsoon period.

The dispersion of the freshwater plume results in the formation of the barrier layer in the BoB. The seasonal evolution of the simulated barrier layer thickness (BLT) for the four simulations is shown in Fig. 12. The sensitivity of the BLT to both wind forcing and river input variation is discussed in brief next. First, the seasonal range of BLT variation is much higher in the northern Bay (10–40 m) than in the southern Bay (10–20 m) (compare panel a with panel b in Fig. 12). In both the northern and southern BOB, between April and November, enhanced mixing due to stronger winds reduces the simulated BLT compared to that when forced by weaker winds. For both wind conditions, the zero-salinity simulations resulted in deeper BLT compared to seasonal salinity runs, by about 5–10 m for the northern Bay, about 2–5 m for the southern Bay, and about 5 m for the entire BoB region over the annual cycle.

4.5. Sensitivity of the coastal upwelling

After diminishing the northeast winter monsoon, the wind direction reverses over the BoB. In April, the southwesterly wind starts blowing only in the western part of the BoB, and the BoB experiences the southwesterly domain-wide from May through September. These southwesterly winds induce an Ekman drift that leads to a band of coastal upwelling along the eastern coast of India. The coastal upwelling brings the colder, saltier, and nutrient-rich subsurface water to the surface. As a result, a band of colder, saltier water with higher chlorophyll-a (chl-a) concentration could be seen along the coastal upwelling regions. Fig. 13 presents evidence of such upwelling signatures from observed GHRSST (Group for High Resolution SST, http://ghrsst.jpl.nasa.gov/) and chl-a from SeaWIFS (Sea-Viewing Wide Field-of-View Sensor). Upwelling regions visible in the GHRSST monthly climatological fields (computed by averaging daily fields over April 2006–December 2015) (Fig. 13, upper panel) agree reasonably well with simulated (CRZ and QRZ) SST fields (middle panels) and SeaWIFS chl-a monthly climatological fields (lower panel). Interestingly, the upwelling generally starts from April, when the cold-water and high-chl-a bands are visible along the coast north of 12°N and extend over almost the entire coast until July–August. This pattern of upwelling-induced SST anomaly matches remarkably well with chl-a during August in the 16–18°N region, which is a clear signature of the formation of the summer blooms in the northwestern BoB induced by coastal upwelling, as was explained by Thushara and Vinayachandran (2016) using a biophysical model. The chl-a signature reaches its maximum extent in August (see the lower panel of Fig. 13) and then begins to diminish until it disappears in December/January (not shown). It is also interesting to note that, during August–September, the wind remains southwesterly and hence upwelling-favorable; however, from August, the upwelling is observed to be suppressed in the northern part of the coast, and there is no upwelling signature north of 18°N in September. This suppression is likely due to the southwest flow that forms the western arm of the NBCG (see Fig. 6, middle column). The impact of the wind strength on the upwelling is evident when comparing the simulations forced by weaker (CRZ) versus stronger (QRZ) winds. The extent and intensity of the cold-water band in the QRZ fields is more prominent and closer to the observation. The stronger winds induce enhanced upwelling results, with an upwelled SST about 0.8 °C cooler, as seen by comparing the upwelling bands of the QRZ fields with those of the QRS fields. The upwelled water in the CRZ (QRZ) fields along the coast is ~0.5 °C (~1.0 °C) colder than the water offshore.

Fig. 14 presents the average vertical structure of the upwelled temperature field during the period June–August across a section similar to Leg E of Shetye et al. (1991b), for both the CRZ and QRZ simulated fields. The upwelling signatures in both simulations, as visible from the up-sloping of the isotherms and isohalines near the coast above 50 m, are in reasonable agreement with the observed upwelling structures during July–August of 1989 as reported by Shetye et al. (1991b; see their Fig. 3) and by Vinayachandran and Kurian (2007). Note that the surface signature of the upwelling is illustrated by the 29 °C isotherm in the CRZ fields, while that signature is represented by 28.5 °C in the QRZ fields, indicating the enhanced nature of upwelling

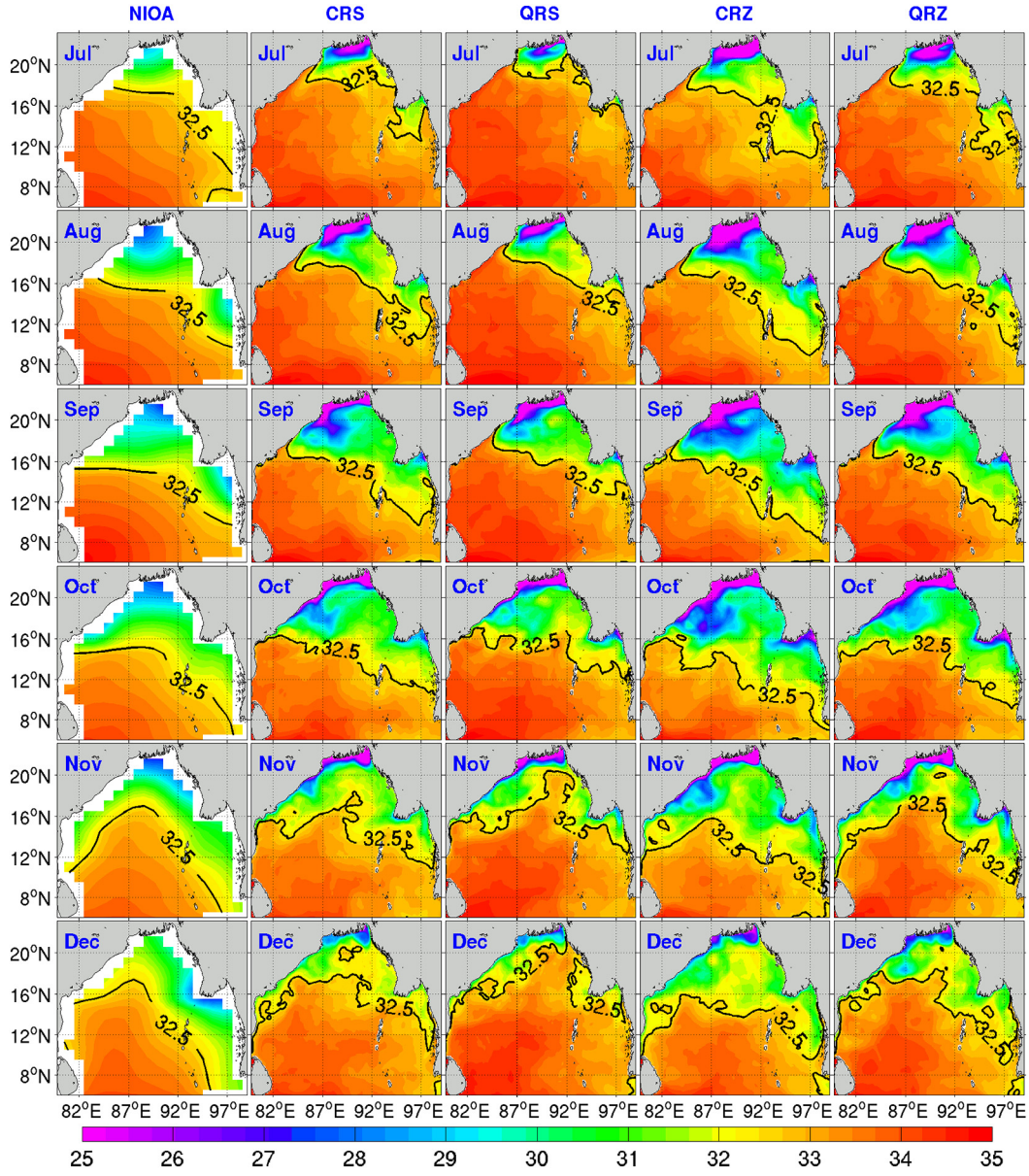

Fig. 10. SSS (psu) from: NIOA (1st column); CRS (2nd column); QRS (3rd column); CRZ (4th column); and, QRZ (5th column) during Jul-Dec. The 32.5 psu contours demarcates the dispersion of freshwater plume.

for the QRZ simulations. Enhanced upwelling leads to a $> 0.6\,^{\circ}C$ colder SST along the major part of the coast in QRZ as compared to CRZ (Fig. 14c).

4.6. Sensitivity to salinity representations near river mouths

Finally, we contrasted the effects of different coastal buoyancy parameterization (seasonally varying estuarine salinity vs. zero salinity) near river mouths. Fig. 15 illustrates the simulated seasonal cycle for the salinity near the GBM mouth. The averaging area is shown in the inset of Fig. 15. The seasonal cycle was determined by computing the box-averaged surface salinity from each simulation and compared against the box-averaged salinity for the NIOA climatology. To be consistent, simulated salinities were averaged over common NIOA grids. Two results are evident from this comparison. First, all the simulated salinities are closer to the climatology during pre-monsoon periods, but diverge from the climatology during the monsoon and post-monsoon periods. Second, the simulations with seasonal salinity inputs (CRS and QRS) generally realized salinity values closer to the climatology, while the zero salinity runs (CRZ and QRZ) over-freshened the ocean, especially the during monsoon and post-monsoon periods.

5. Discussion

The basin-scale validation of the simulated annual mean fields and seasonal variabilities in all four configurations shows reasonable agreement with the climatologies (Figs. 2–4 and Table 3); however, the skill of the modeling system in capturing the seasonal variabilities is heterogeneous in space (Fig. 4). This is normal since some mesoscale features are present in the averaged model simulations. The skills for SST and SSS were high in all the simulations. Note that despite the absence of relaxation (with a typical decay-scale of 30 to 120 days) of SSS to the climatology, the simulated SSS in all the simulations shows reasonable agreement with observation in reproducing the spatial and seasonal patterns; however, the simulated variabilities are due to varying winds and river input conditions.

Interestingly, the impact of stronger winds resulted in relative cooling (and salting) near the surface and relative warming (and

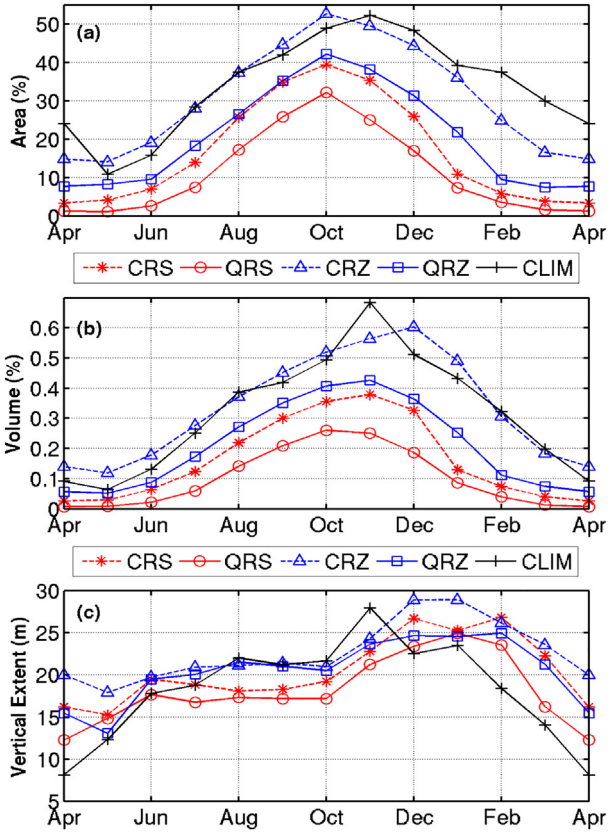

Fig. 11. Seasonal evolution of (a) area, (b) volume, and (c) vertical extension of the freshwater plume region (as defined by the 32.5 psu contour in 3-D). Note the 1-month lag in reaching the peak value for volume coverage from area coverage and then for mean vertical extent from the volume coverage.

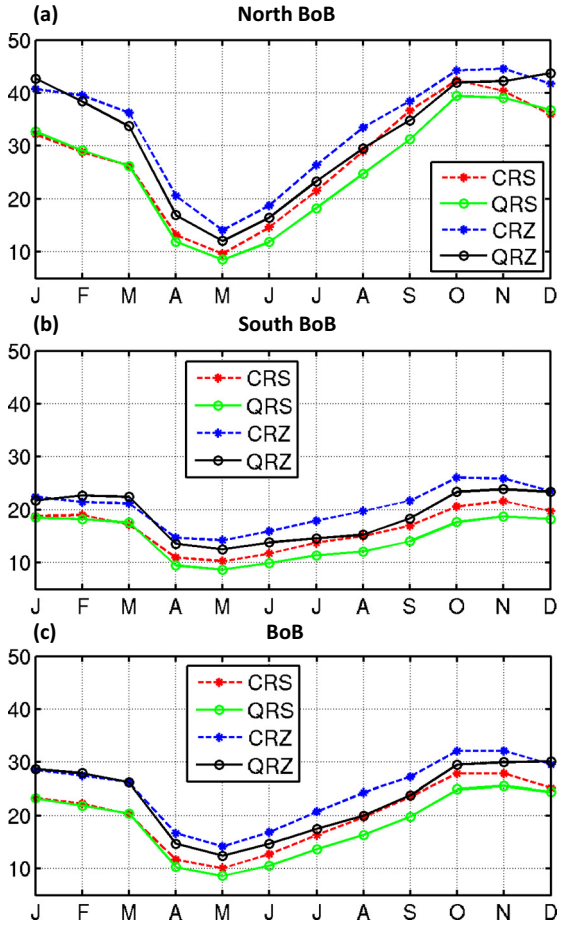

Fig. 12. Annual cycles of barrier layer thickness (BLT) in m averaged over (a) northern BoB, (b) southern BoB and (c) entire BoB from CRS, QRS, CRZ and QRZ. Note the higher seasonal range exhibited in the north compared to the south and over the entire BoB. See text for other details.

freshening) below the mixed layer. The increase of surface salinity was due to wind-induced enhanced mixing of subsurface saltier water with fresher near-surface layers. Thus, stronger wind simulations yielded higher MLD skills compared to their weaker-wind counterparts for a fixed-buoyancy input (either zero or seasonal salinity). The fresher river inflow also increased the MLD skill for a fixed wind (either strong or weak) simulation when compared to the seasonal salinity case. The skill increases in both cases were almost 10% (see Table 3). As expected, stronger winds (added freshness) have a significant negative (minimal) impact on the SSH skill.

From a circulation perspective, stronger winds resulted in a stronger springtime WBC and a strong anticyclonic eddy at around 12°N, 82°E, while enhancing the Ekman-drift-induced eastward flow over the domain during summer monsoon. The southwest monsoon current was mostly insensitive to either wind or buoyancy variations, indicative of its robustness due to boundary conditions and other dynamical factors in these simulations. For the four simulations, the simulated EICC was a weaker and narrower current meandering alongside multiple mesoscale eddies when compared to its OSCAR representation. Our findings show that the EKE is primarily wind-driven during the year and gets modulated by buoyancy forcing, with a reducing effect in summer and enhancing impact in autumn and winter. This result could help in future quantification and understanding of biogeochemical processes, as they would have to be driven by different physical processes (wind-induced upwelling vs. buoyancy-induced nutrient transport) at different times of the year.

As expected, the fresher buoyancy flux reduces the domain-wide salinity; however, the temperature remains mostly unaltered. For either the zero or seasonal salinity river forcing, the stronger-wind simulations always resulted in higher volume-averaged salinity than did their weaker-wind counterparts. This is probably due to the stronger wind-induced enhanced transport through the western boundaries; for example, the transport of the SMC for the stronger winds was about 4 Sv larger in the upper 100 m than in the weaker-wind case for both salinity-fixed sets of runs. Fresher buoyancy forcing resulted in a more pronounced near-surface stability maximum in the northern Bay. Note that none of the simulations showed a near-surface maximum in the southern Bay averaged stratification, indicating the constrained nature of the dominant impact of river runoffs that is limited to the northern Bay, irrespective of the wind or buoyancy variations.

The strength, growth, and freshness of the EICC increased with the fresher river buoyancy flux, with fresher river inputs widening the spatial and vertical extent of the plume. Interestingly, stronger winds did not increase the spreading of the plume, but rather reduced the area and volume due to enhanced mixing. Coastal upwelling was simulated for all the runs throughout the upwelling-favorable southwesterly wind regime (April through September) along the east coast of India. The upwelling is mostly seen along the northern part of the coast during April–May, gradually extending along the entire coast during June–July, but by August, the upwelling was suppressed in the northern part.

6. Conclusion

In this study, we presented a sensitivity analysis of the Bay of Bengal (BoB) climatological thermohaline structure and circulation to two different wind forcings (weaker COADS and stronger QuikSCAT) and

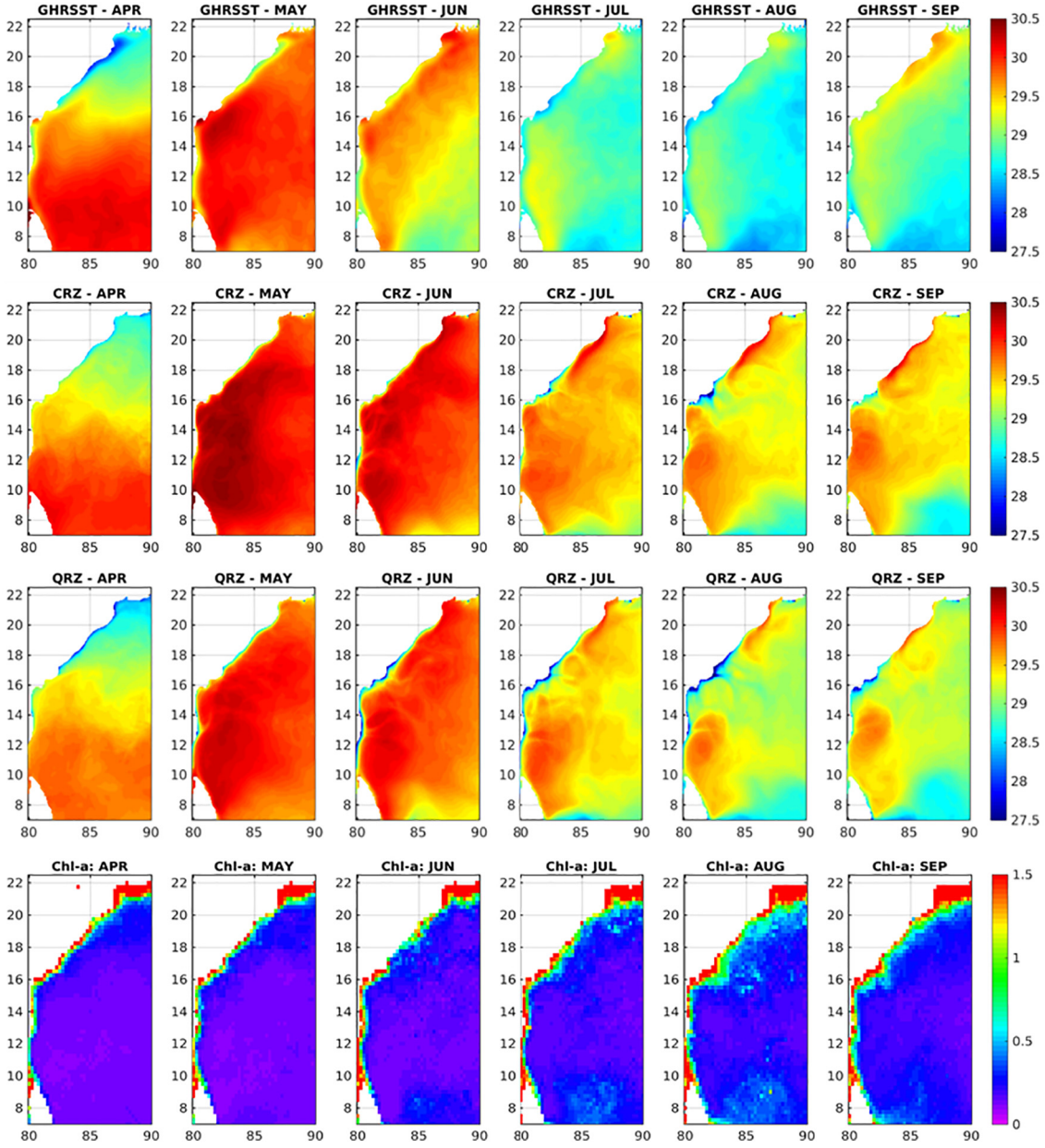

Fig. 13. Coastal upwelling signature as visible in the observed (top row) and simulated (CRZ: 2nd row and QRZ: 3rd row) SST (°C) fields and in the observed SeaWIFS chlorophyll-a concentration (mg/m^3 in log scale) fields during April–September (columns from left to right respectively). The narrow blue patches of cold water and high chlorophyll-a concentration along the east coast in all the panels are due to the coastal upwelling. See text for details. (For interpretation of the references to color in this figure legend, the reader is referred to the web version of this article.)

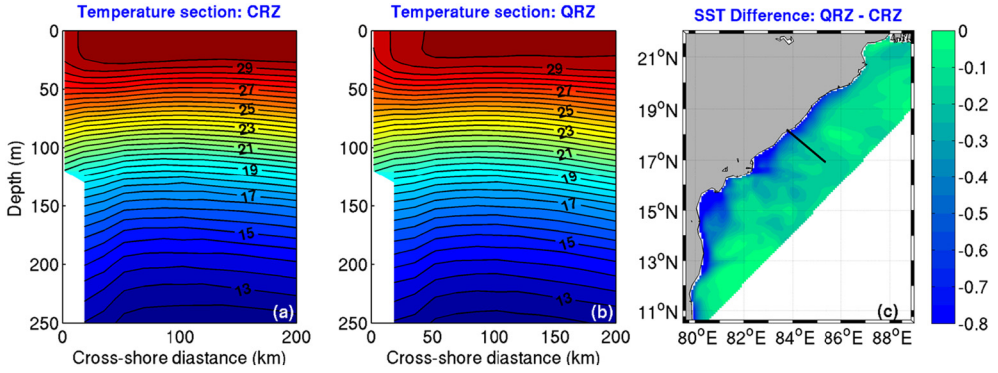

Fig. 14. Signature of coastal upwelling: vertical sections in the temperature (°C) fields of the (a) CRZ and (b) QRZ fields; and SST difference (c) between CRZ and QRZ. The black line near 18°N in (c) denotes the location of the cross-shore section, which is similar to Leg E of Shetye (1993). All the fields presented here are the average of Jun–Aug fields.

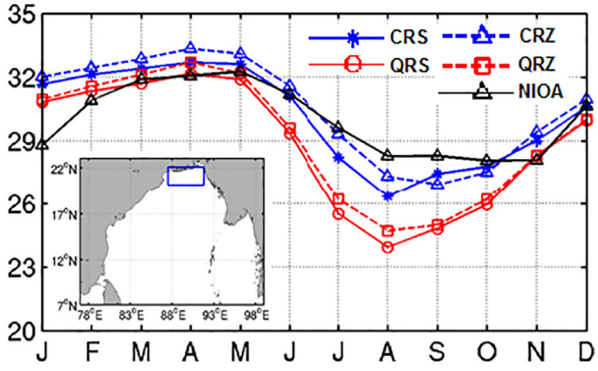

Fig. 15. Annual cycle of SSS (psu) averaged over a Box (blue box in the inset plot) near the mouth of GBM for the four simulations, compared against that from the NIOA climatology. For consistency, the computations are carried out on NIOA grid and land mask. Note that both of the zero salinity runs significantly underestimate the seasonal cycle of climatology during June through October. (For interpretation of the references to color in this figure legend, the reader is referred to the web version of this article.)

two different representations of river inputs (zero salinity or a seasonal estuarine salinity cycle), using an eddy-resolving ROMS setup. The spatial distribution of the annual evolving fields of SST, SSS, SSH, and MLD shows high average correlation (> 0.7) when compared to NIOA climatology. Stronger winds (fresher river inflow) increased the MLD skill by almost 10% for fixed river input (fixed wind condition) and have a significant negative (minimal) impact on the SSH skill.

Our results indicated that stronger winds lower the SST and plume dispersion and enhance SSS. The upwelling's regional extent and vertical steepness (amplitude) both increased with stronger winds. The purely fresh river input brought the simulated domain-wide salinity closer to reality and hence the simulated MLD, stratification and BLT became more realistic; however, it significantly underestimated the local salinity of the coastal regions near the river mouths, where the estuarine salinity river input simulated more realistic salinity. The estuarine salinity river representation can be further improved by imposing more accurate salinity seasonal cycles and by accounting for proper vertical distribution of estuarine flow (inflow-outflow; Han and McCreary, 2001) at the river mouths. Developing such accurate salinity representation could utilize a combination of practical and theoretical approaches involving at least the following: (i) new satellite missions for observing salinity, (ii) dedicated observational monitoring programs near major river mouths and (iii) high-resolution, coupled, ocean-estuarine regional models, with special attention to vertical distribution of fluxes and cross-shelf and nearshore exchange processes.

Our sensitivity results should be useful for future high-resolution simulations in the Bay of Bengal. Future studies should surpass the skills presented here through improved parameterizations; more accurate river discharges and tidal forcing; advanced multiscale and multivariate data assimilation (Gangopadhyay et al., 2012; Lermusiaux et al., 2011, 2013; Miyazawa et al., 2015); and adaptive data collection (Lermusiaux, 2007; Lermusiaux et al., 2016). More accurate river discharge models (e.g., Whitney and Garvine, 2006; Banas et al., 2009; Mirabito et al., 2012) will help resolve coastal and shelf circulation, shelf-slope exchanges, and cross-shelf transport, which are all important for understanding the impact of climate change on the coastal ecosystem and fisheries at large. Targeted multiscale (large-scale to submesoscale) synoptic observational studies would provide multiscale validation and allow such improved modeling systems to become operational. The sensitivities to strong/weak winds and river buoyancy forcing could be helpful to diagnose the corresponding interannual variability. A systematic study to understand the sensitivity of the model results to varying vertical resolution while keeping high horizontal resolution has not been done yet for the Bay. Recent simulations (Lermusiaux et al., 2017) show that such effects can be significant. Integrated observational and modeling studies should be carefully designed for resolving multiscale features in space and time, and for understanding short-term and long-term variability of the region within a changing climate.

Acknowledgments

The altimeter products were produced by Ssalto/Duacs and distributed by AVISO, with support from CNES. AG and SJ acknowledge the support of the Fulbright-Nehru Foundation for initiating this study. PFJL, SJ, and PJH are grateful to the Office of Naval Research (ONR) for research support under grant N00014-15-1-2616 (NASCar-OPS) to the Massachusetts Institute of Technology (MIT) as well as to the Tata Center at MIT for funding part of this work. SS acknowledges the help from Mr. Saikat Pramanik and partial financial support from Science and Engineering Research Board (SERB), Government of India. We sincerely thank Mr. Frank Smith of SMAST for carefully editing the revised manuscript. Finally, we are grateful to the two reviewers and the Editor for their thoughtful suggestions that greatly helped to improve the quality of the paper.

References

Akhil, V.P., Durand, F., Lengaigne, M., Vialard, J., Keerthi, M.G., Gopalakrishna, V.V., Deltel, C., Papa, F., de Boyer Montégut, C., 2014. A modeling study of the processes of surface salinity seasonal cycle in the Bay of Bengal. J. Geophys. Res. 119 (6), 3926–3947.

Balaguru, K., Chang, P., Saravanan, R., Leung, L.R., Xu, Z., Li, M., Hsieh, J.S., 2012. Ocean barrier layers' effect on tropical cyclone intensification. Proc. Natl. Acad. Sci. 109 (36), 14343–14347.

Banas, N.S., MacCready, P., Hickey, B.M., 2009. The Columbia River plume as cross-shelf exporter and along-coast barrier. Cont. Shelf Res. 29, 292–301.

Behara, A., Vinayachandran, P.N., 2016. An OGCM study of the impact of rain and river water forcing on the Bay of Bengal. J. Geophys. Res. Oceans 121 (4), 2425–2446.

Benshila, R., Durand, F., Masson, S., Bourdall-Badie, R., de Boyer Montgut, C., Papa, F., Madec, G., 2014. The upper Bay of Bengal salinity structure in a high-resolution model. Ocean Model. 74, 36–52.

Boyer, T., Levitus, S., Garcia, H., Locarnini, R., Stephens, C., Antonov, J., 2005. Objective analyses of annual, seasonal, and monthly temperature and salinity for the world ocean on a 1/4° grid. Int. J. Climatol. 25, 931–945.

Capotondi, A., Combes, V., Alexander, M.A., Di Lorenzo, E., Miller, A.J., 2009. Low-frequency variability in the Gulf of Alaska from coarse and eddy-permitting ocean models. J. Geophys. Res. Oceans 114 (C01017). https://doi.org/10.1029/2008JC004983.

Chamarthi, S., Shree Ram, P., Josyula, L., 2008. Effect of river discharge on bay of Bengal circulation. Mar. Geod. 31 (3), 160–168. https://doi.org/10.1080/01490410802265476.

Chatterjee, A., Shankar, D., Shenoi, S.S.C., Reddy, G.V., Michael, G.S., Ravichandran, M., Gopalkrishna, V.V., Rao, E.P.R., Bhaskar, T.V.S.U., Sanjeevan, V.N., 2012. A new atlas of temperature and salinity for the North Indian Ocean. J. Earth Syst. Sci. 121 (3), 559–593.

Chen, D., Liu, W.T., Zebiak, S.E., Cane, M.A., Kushnir, Y., Witter, D., 1999. Sensitivity of the tropical Pacific Ocean simulation to the temporal and spatial resolution of wind forcing. J. Geophys. Res. Oceans 104 (C5), 11261–11271.

Chowdary, J.S., Srinivas, G., Fousiya, T.S., Parekh, A., Gnanaseelan, C., Seo, H., MacKinnon, J.A., 2016. Representation of Bay of Bengal upper-ocean salinity in general circulation models. Oceanography 29 (2), 38–49.

Cutler, A.N., Swallow, J.C., 1984. Surface Currents of the Indian Ocean (to 25°S to 100°E). Report No. 87. Institute of Oceanographic Sciences, Broadchill, UK.

da Silva, A.M., Young, C.C., Levitus, S., 1994. Atlas of surface marine data 1994. In: Algorithms and Procedures. vol. 1 NOAA Atlas NESDIS 6, U.S. Department of Commerce, NOAA, NESDIS.

de Boyer Montégut, C., Vialard, J., Shenoi, S.S.C., Shankar, D., Durand, F., Ethé, C., Madec, G., 2007. Simulated seasonal and interannual variability of mixed layer heat budget in the northern Indian Ocean. J. Clim. 20, 3249–3268.

Durand, F., Shankar, D., Birol, F., Shenoi, S.S.C., 2008. Estimating boundary currents from satellite altimetry: a case study for the east coast of India. J. Oceanogr. 64, 831–845.

Durand, F., Shankar, D., Birol, F., Shenoi, S.S.C., 2009. Spatiotemporal structure of the East India Coastal Current from satellite altimetry. J. Geophys. Res. 114, C02013. https://doi.org/10.1029/2008JC004807.

Durand, F., Papa, F., Rahman, A., Bala, S.K., 2011. Impact of Ganges–Brahmaputra interannual discharge variations on Bay of Bengal salinity and temperature during 1992–1999 period. J. Earth Syst. Sci. 120 (5), 859–872.

Fairall, C.W., Bradley, E.F., Rogers, D.P., Edson, J.B., Young, G.S., 1996. Bulk parameterization of air–sea fluxes for tropical ocean–global atmosphere coupled-ocean atmosphere response experiment. J. Geophys. Res. 101 (C2), 3747–3764.

Fekete, B.M., Vorosmarty, C.J., Grabs, W., 2000. Global, composite runoff fields based on observed river discharge and simulated water balances. In: Documentation for UNHGRDC Composite Runoff Fields, v.1.0. Global Runoff Data Center, Koblenz, Germany.

Gangopadhyay, A., Schmidt, A., Agel, L., Schofield, O., Clark, J., 2012. Multiscale forecasting in the Western North Atlantic: Sensitivity of model forecast skill to glider data assimilation. Cont. Shelf Res. https://doi.org/10.1016/j.csr.2012.09.013.

Gangopadhyay, A., Bharat Raj, G.N., Chaudhuri, A.H., Babu, M.T., Sengupta, D., 2013. On the nature of meandering of the springtime western boundary current in the Bay of Bengal. Geophys. Res. Lett. 40, 2188–2193. https://doi.org/10.1002/grl.50412.

Girishkumar, M.S., Ravichandran, M., Han, W., 2013. Observed intraseasonal thermocline variability in the Bay of Bengal. J. Geophys. Res. Oceans 118 (7), 3336–3349.

Gopalakrishna, V.V., Murty, V.S.N., Sengupta, D., Shenoy, S., Araligidad, N., 2002. Upper ocean stratification and circulation in the northern Bay of Bengal during southwest monsoon of 1991. Cont. Shelf Res. 22 (5), 791–802.

Haidvogel, D.B., Arango, H.G., Hedstrom, K., Beckmann, A., Malanotte-Rizzoli, P., Shchepetkin, A.F., 2000. Model evaluation experiments in the North Atlantic basin: Simulations in nonlinear terrain-following coordinates. Dyn. Atmos. Oceans 32, 239–281.

Haley Jr., P.J., Lermusiaux, P.F.J., 2010. Multiscale two-way embedding schemes for free-surface primitive-equations in the Multidisciplinary Simulation, Estimation and Assimilation System. Ocean Dyn. 60, 1497–1537. https://doi.org/10.1007/s10236-010-0349-4.

Haley, P.J., Agarwal, A., Lermusiaux, P.F.J., 2015. Optimizing velocities and transports for complex coastal regions and archipelagos. Ocean Model. 89, 1–28. https://doi.org/10.1016/j.ocemod.2015.02.005.

Han, W., McCreary, J.P., 2001. Modeling salinity distributions in the Indian Ocean. J. Geophys. Res. 106, 859–877.

Hastenrath, S., Greischar, L., 1991. The monsoonal current regimes of the tropical Indian Ocean: observed surface flow fields and their geostrophic and wind-driven components. J. Geophys. Res. 96 (C7), 12619–12633. https://doi.org/10.1029/91JC00997.

Haugen, V.E., Johannessen, O.M., Evensen, G., 2002. Indian ocean: validation of the Miami isopycnic coordinate ocean model and ENSO events during 1958–1998. J. Geophys. Res. 107 (C5). https://doi.org/10.1029/2000JC000330.

Hellerman, S., Rosenstein, M., 1983. Normal monthly wind stress over the world ocean with error estimates. J. Phys. Oceanogr. 13 (7), 1093–1104.

Hogan, P.J., Hurlburt, H.E., 2005. Sensitivity of simulated circulation dynamics to the choice of surface wind forcing in the Japan/East Sea. Deep-Sea Res. II Top. Stud. Oceanogr. 52 (11 – 13), 1464–1489.

Hong, B., Wang, D., 2008. Sensitivity study of the seasonal mean circulation in the northern South China Sea. Adv. Atmos. Sci. 25 (5), 824–840.

Howden, S.D., Murtugudde, R., 2001. Effects of river inputs into the Bay of Bengal. J. Geophys. Res. 106 (C9), 19825–19843.

Jana, S., 2014. Ocean State Simulation of the Bay of Bengal with River Input Using Regional Ocean Modeling System (ROMS) (Ph.D dissertation). IIT Kharagpur, India.

Jana, S., Gangopadhyay, A., Chakraborty, A., 2015. Impact of seasonal river input on the Bay of Bengal simulation. Cont. Shelf Res. 104, 45–62.

Jensen, T.G., 2011. Bifurcation of the Pacific North equatorial current in a wind-driven model: response to climatological winds. Ocean Dyn. 61 (9), 1329–1344.

Jensen, T.G., Wijesekera, H.W., Nyadjro, E.S., Thoppil, P.G., Shriver, J.F., Sandeep, K.K., Pant, V., 2016. Modeling salinity exchanges between the equatorial Indian Ocean and the Bay of Bengal. Oceanography 29 (2), 92–101.

Kantha, L.H., Clayson, C.A., 2000. Numerical models of oceans and oceanic processes. vol. 66 Elsevier (750 pp.).

Kersale, M., Doglioli, A.M., Petrenko, A.A., 2011. Sensitivity study of the generation of mesoscale eddies in a numerical model of Hawaii islands. Ocean Sci. 7 (3), 277–291.

Large, W.G., McWilliams, J.C., Doney, S.C., 1994. Oceanic vertical mixing: a review and a model with a nonlocal boundary layer parameterization. Rev. Geophys. 32, 363–403.

Legeckis, R., 1987. Satellite observations of a western boundary current in the Bay of Bengal. J. Geophys. Res. 92, 12974–12978.

Lermusiaux, P.F.J., 2007. Adaptive modeling, adaptive data assimilation and adaptive sampling. Refereed invited manuscript. In: Jones, C.K.R.T., Ide, K. (Eds.), Special issue on “Mathematical Issues and challenges in Data Assimilation for Geophysical Systems: Interdisciplinary Perspectives”. Physica D, vol 230. pp. 172–196. https://doi.org/10.1016/j.physd.2007.02.014.

Lermusiaux, P.F.J., Haley Jr., P.J., Leslie, W.G., Agarwal, A., Logutov, O.G., Burton, L.J., 2011. Multiscale physical and biological dynamics in the Philippine Archipelago: predictions and processes. Oceanography 24 (1), 70–89. https://doi.org/10.5670/oceanog.2011.05.

Lermusiaux, P.F.J., Schröter, J., Danilov, S., Iskandarani, M., Pinardi, N., Westerink, J.J., 2013. Multiscale modeling of coastal, shelf and global ocean dynamics. Ocean Dyn. 63, 1341–1344. https://doi.org/10.1007/s10236-013-0655-8.

Lermusiaux, P.F.J., Lolla, T., Haley Jr., P.J., Yigit, K., Ueckermann, M.P., Sondergaard, T., Leslie, W.G., 2016. Science of autonomy: time-optimal path planning and adaptive sampling for swarms of ocean vehicles. In: Curtin, Tom (Ed.), Chapter 21, Springer Handbook of Ocean Engineering: Autonomous Ocean Vehicles, Subsystems and Control, pp. 481–498. https://doi.org/10.1007/978-3-319-16649-0_21.

Lermusiaux, P.F.J., Haley Jr., P.J., Jana, S., Gupta, A., Kulkarni, C.S., Mirabito, C., Ali, W.H., Subramani, D.N., Dutt, A., Lin, J., Shcherbina, A.Y., Lee, C.M., Gangopadhyay, A., 2017. Optimal planning and sampling predictions for autonomous and Lagrangian platforms and sensors in the northern Arabian Sea. Oceanography 30 (2), 172–185.

Levin, J., Wilkin, J., Fleming, N., Zavala-Garay, J., 2018. Mean circulation of the Mid-Atlantic Bight from a climatological data assimilative model. Ocean Model 128, 1–14.

Lucas, A.J., Nash, J.D., Pinkel, R., MacKinnon, J.A., Tandon, A., Mahadevan, A., Omand, M.M., Freilich, M., Sengupta, D., Ravichandran, M., Le Boyer, A., 2016. Adrift upon a salinity-stratified sea: a view of upper-ocean processes in the Bay of Bengal during the southwest monsoon. Oceanography 29 (2), 134–145.

Mahadevan, A., Jaeger, G.S., Freilich, M., Omand, M.M., Shroyer, E.L., Sengupta, D., 2016. Freshwater in the Bay of Bengal: its fate and role in air-sea heat exchange. Oceanography 29 (2), 72–81.

Manyilizu, M., Dufois, F., Penven, P., Reason, C., 2014. Interannual variability in the tropical western Indian Ocean. Afr. J. Mar. Sci. 36 (2), 233–252.

Marchesiello, P., McWilliams, J.C., Shchepetkin, A.F., 2001. Open boundary conditions for long-term integration of regional ocean models. Ocean Model. 3, 1–20.

McCreary Jr., J.P., Kundu, P.K., Molinari, R.L., 1993. A numerical investigation of dynamics, thermodynamics and mixed layer processes in the Indian Ocean. Prog. Oceanogr. 31, 181–244. https://doi.org/10.1016/0079-6611(93)90002-U.

Metzger, E.J., 2003. Upper ocean sensitivity to wind forcing in the South China Sea. J. Oceanogr. 59 (6), 783–798.

Mirabito, C., Haley Jr., P.J., Lermusiaux, P.F.J., Leslie, W.G., 2012. A River Discharge Model for Coastal Taiwan During Typhoon Morakot. MSEAS Report-13, August 2012.

Miyazawa, Y., Guo, X., Varlamov, S.M., Miyama, T., Yoda, K., Sato, K., Kano, T., Sato, K., 2015. Assimilation of the seabird and ship drift data in the north-eastern sea of Japan into an operational ocean nowcast/forecast system. Sci. Rep. 5, 17672.

Neetu, S., Lengaigne, M., Vincent, E.M., Vialard, J., Madec, G., Samson, G., Ramesh Kumar, M.R., Durand, F., 2012. Influence of upper-ocean stratification on tropical cyclone-induced surface cooling in the Bay of Bengal. J. Geophys. Res. Oceans 117 (C12). https://doi.org/10.1029/2012JC008433.

Orlanski, I., 1976. A simple boundary condition for unbounded hyperbolic flows. J. Comput. Sci. 21 (3), 251–269.

Pant, V., Girishkumar, M.S., Udaya Bhaskar, T.V.S., Ravichandran, M., Papa, F., Thangaprakash, V.P., 2015. Observed interannual variability of near-surface salinity in the Bay of Bengal. J. Geophys. Res. Oceans 120 (5), 3315–3329.

Paulson, C.A., Simpson, J.J., 1977. Irradiance measurements in the upper ocean. J. Phys. Oceanogr. 7 (6), 952–956.

Penven, P., Debreu, L., Marchesiello, P., McWilliams, J.C., 2006. Evaluation and application of the ROMS 1-way embedding procedure to the central California upwelling system. Ocean Model. 12, 157–187.

Pond, S., Pickard, G.L., 1983. Introductory Dynamic Oceanography. Pergamon, New York, pp. 241.

Prasanna Kumar, S., Muraleedharan, P.M., Prasad, T.G., Gauns, M., Ramaiah, N., de Souza, S.N., Sardesai, S., Madhupratap, M., 2002. Why is the Bay of Bengal less productive during summer monsoon compared to the Arabian Sea? Geophys. Res. Lett. 29 (24), 2235. https://doi.org/10.1029/2002GL016013.

Praveen Kumar, B., Vialard, J., Lengaigne, M., Murty, V.S.N., McPhaden, M.J., Cronin, M.F., Gopala Reddy, K., 2013. TropFlux Surface wind stress over the tropical oceans: Comparisons and evaluations. Clim. Dyn. 40 (7–8), 2049–2071.

Rahaman, W., Singh, S.K., Shukla, A.D., 2012. Rhenium in Indian rivers: sources, fluxes, and contribution to oceanic budget. Geochem. Geophys. Geosyst. 13 (Q08019). https://doi.org/10.1029/2012GC004083.

Rahaman, H., Ravichandran, M., Sengupta, D., Harrison, M.J., Griffies, S.M., 2014. Development of a regional model for the North Indian Ocean. Ocean Model. 75, 1–19.

Rao, A.D., Dash, S., Jain, I., Dube, S.K., 2007. Effect of estuarine flow on ocean circulation using a coupled coastal-bay estuarine model: an application to the 1999 Orissa cyclone. Nat. Hazards 41 (3), 549–562.

Risien, C.M., Chelton, D.B., 2008. A global climatology of surface wind and wind stress fields from eight years of QuikSCAT scatterometer data. J. Phys. Oceanogr. 38, 2379–2413. https://doi.org/10.1175/2008JPO3881.1.

Riverside Technology Inc. (RTi), Center for Environmental and Geographic Information Services (CEGIS), Bangladesh Disaster Preparedness Center (BDPC), 2008. Community Flood Information System. Final Report. Prepared for United States Agency for International Development (USAID).

Sadhuram, Y., Sarma, V.V., Murthy, T.V.R., Rao, B.P., 2005. Seasonal variability of physico–chemical characteristics of the Haldia channel of Hooghly estuary, India. J. Earth Syst. Sci. 114 (1), 37–49.

Satheesan, K., Sarkar, A., Parekh, A., Ramesh Kumar, M.R., Kuroda, Y., 2007. Comparison of wind data from QuikSCAT and buoys in the Indian Ocean. Int. J. Remote Sens. 28, 2375–2382.

Schmidt, A., Gangopadhyay, A., 2013. An operational ocean circulation prediction system for the western North Atlantic: hindcasting during July–September of 2006. Cont. Shelf Res. 63, S177–S192.

Schott, F.A., Xie, S.P., McCreary, J.P., 2009. Indian Ocean circulation and climate variability. Rev. Geophys. 47, RG1002. https://doi.org/10.1029/2007RG000245.

Sengupta, D., Goddalehundi, B.R., Anitha, D.S., 2008. Cyclone-induced mixing does not cool SST in the post-monsoon North Bay of Bengal. Atmos. Sci. Lett. 9 (1), 1–6.

Sengupta, D., Bharath Raj, G.N., Ravichandran, M., Sree Lekha, J., Papa, F., 2016. Near-surface salinity and stratification in the north Bay of Bengal from moored observations. Geophys. Res. Lett. 43 (9), 4448–4456.

Seo, H., Xie, S.-P., Murtugudde, R., Jochum, R., Miller, A., 2009. Seasonal effects of Indian Ocean fresh water forcing in a regional coupled model. J. Clim. 22, 6577–6596.

Shankar, D., McCreary, J.P., Han, W., Shetye, S.R., 1996. Dynamics of the East India coastal current: 1. Analytic solutions forced by interior Ekman pumping and local alongshore winds. J. Geophys. Res. 101 (C6), 13975–13991. https://doi.org/10.1029/96JC00559.

Shankar, D., Vinayachandran, P.N., Unnikrishnan, A.S., 2002. The monsoon currents in the north Indian Ocean. Prog. Oceanogr. 52, 63–120.

Sharma, R., Agarwal, N., Momin, I.M., Basu, S., Agarwal, V.K., 2010. Simulated sea surface salinity variability in the tropical Indian Ocean. J. Clim. 23 (24), 6542–6554.

Shchepetkin, A.F., McWilliams, J.C., 2003. A method for computing horizontal pressure–gradient force in an oceanic model with a nonaligned vertical coordinate. J. Geophys. Res. 108 (C3), 3090. https://doi.org/10.1029/2001JC001047.

Shchepetkin, A.F., McWilliams, J.C., 2005. The regional oceanic modeling system: a

split–explicit, free-surface, topography-following-coordinate ocean model. Ocean Model. 9, 347–404.
Shetye, S.R., 1993. The movement and implications of the Ganges–Bramhaputra runoff on entering the Bay of Bengal. Curr. Sci. 64 (1), 32–38.
Shetye, S.R., Gouveia, A.D., Shenoi, S.S.C., Sundar, D., Michael, G.S., Almeida, A.A., Santanam, K., 1991a. The coastal currents off western India during northeast monsoon. Deep-Sea Res. I 38 (12), 1517–1529.
Shetye, S.R., Shenoi, S.S.C., Gouveia, A.D., Michael, G.S., Sundar, D., Nampoothiri, G., 1991b. Wind driven coastal upwelling along the western boundary of the Bay of Bengal. Cont. Shelf Res. 11, 1397–1408. https://doi.org/10.1016/0278-4343(91)90042-5.
Shetye, S.R., Gouveia, A.D., Shenoi, S.S.C., Shankar, D., Vinayachandran, P.N., Sundar, D., Michael, G.S., Nampothiri, G., 1996. Hydrography and circulation in the western Bay of Bengal during the northeast monsoon. J. Geophys. Res. 101 (C6), 14011–14025. https://doi.org/10.1029/95JC03307.
Smith, W.H.F., Sandwell, D.T., 1997. Global sea floor topography from satellite altimetry and ship depth soundings. Science 277 (5334), 1956–1962.
Srivastava, A., Dwivedi, S., Mishra, A.K., 2016. Intercomparison of high-resolution Bay of Bengal circulation models forced with different winds. Mar. Geod. 39 (3–4), 271–289.
Strub, P.T., James, C., Combes, V., Matano, R.P., Piola, A.R., Palma, E.D., Saraceno, M., Guerrero, R.A., Fenco, H., Etcheverry, L.A.R., 2015. Altimeter-derived seasonal circulation on the southwest Atlantic shelf: 27 S–43 S. J. Geophys. Res. Oceans 120, 3391–3418. https://doi.org/10.1002/2015JC010769.
Suryanarayana, A., Murty, V.S.N., Rao, D.P., 1993. Hydrography and circulation of the Bay of Bengal during early winter, 1983. Deep-Sea Res. I Oceanogr. Res. Pap. 40 (1), 205–217. https://doi.org/10.1016/0967-0637(93)90061-7.
Syvitski, J.P.M., Vörösmarty, C.J., Kettner, A.J., Green, P., 2005. Impact of humans on the flux of terrestrial sediment to the global coastal ocean. Science 308, 376–380.
Taylor, K.E., 2001. Summarizing multiple aspects of model performance in a single diagram. J. Geophys. Res. 106 (D7), 7183–7192.
Thadathil, P., Gopalakrishna, V.V., Muraleedharan, P.M., Reddy, G.V., Araligidad, N., Shenoy, S., 2002. Surface layer temperature inversion in the Bay of Bengal. Deep-Sea Res. I 49 (10), 1801–1818.
Thadathil, P., Muraleedharan, P.M., Rao, R.R., Somayajulu, Y.K., Reddy, G.V., Revichandran, C., 2007. Observed seasonal variability of barrier layer in the Bay of Bengal. J. Geophys. Res. 112, C02009. https://doi.org/10.1029/2006JC003651.
Thushara, V., Vinayachandran, P.N., 2016. Formation of summer phytoplankton bloom in the northwestern Bay of Bengal in a coupled physical-ecosystem model. J. Geophys. Res. Oceans 121 (12), 8535–8550.
Varkey, M.J., Murty, V.S.N., Suryanarayana, A., 1996. Physical oceanography of the Bay of Bengal and Andaman Sea. In: Ansell, A.D., Gibson, R.N., Barnes, M. (Eds.), Oceanography and Marine Biology: An Annual Review, pp. 34–70.
Vic, C., Roullet, G., Carton, X., Capet, X., 2014. Mesoscale dynamics in the Arabian Sea and a focus on the Great Whirl life cycle: a numerical investigation using ROMS. J. Geophys. Res. Oceans. https://doi.org/10.1002/2014JC009857.
Vinayachandran, P.N., Kurian, J., 2007. Hydrographic observations and model simulation of the Bay of Bengal freshwater plume. Deep-Sea Res. I 54, 471–486.
Vinayachandran, P.N., Murty, V.S.N., Ramesh Babu, V., 2002. Observations of barrier layer formation in the Bay of Bengal during summer monsoon. J. Geophys. Res. Oceans 107 (C12).
Vorosmarty, C.J., Fekete, B.M., Tucker, B.A., 1998. Global River Discharge Database (RivDis) V.1.1.
Whitney, M.M., Garvine, R.W., 2006. Simulating the delaware bay buoyant outflow: comparison with observations. J. Phys. Oceanogr. 36, 3–21.
Wilson, E.A., Riser, S.C., 2016. An assessment of the seasonal salinity budget for the upper Bay of Bengal. J. Phys. Oceanogr. 46 (5), 1361–1376.
Wyrtki, K., 1971. Oceanographic Atlas of the International Indian Ocean Expedition. Nat. Sci. Found., Washington, D.C., pp. 531.
Yeager, S.G., Large, W.G., 2008. CORE.2 global air–sea flux dataset. In: Research Data Archive at the National Center for Atmospheric Research. Computational and Information Systems Laboratory. https://doi.org/10.5065/D6WH2N0S.
Yu, L., Weller, R.A., 2007. Objectively analyzed air–sea heat fluxes for the global ice-free oceans (1981–2005). Bull. Am. Meteorol. Soc. 88, 527–539.
Yu, L., Jin, X., Weller, R.A., 2008. Multidecade Global Flux Datasets from the Objectively Analyzed Air–Sea Fluxes (OAFlux) Project: Latent and Sensible Heat Fluxes, Ocean Evaporation, and Related Surface Meteorological Variables. Woods Hole Oceanographic Institution, OAFlux Project Technical Report, OA-2008-01 (64 pp.).
Zhang, Y., Rossow, W.B., Lacis, A.A., Oinas, V., Mishchenko, M.I., 2004. Calculation of radiative fluxes from the surface to top of atmosphere based on ISCCP and other global data sets: refinements of the radiative transfer model and the input data. J. Geophys. Res. Atmos. 109 (D19). https://doi.org/10.1029/2003JD004457.